Correction notice

Estimates of volcanic-induced cooling in the Northern Hemisphere over the past 1,500 years

Markus Stoffel, Myriam Khodri, Christophe Corona, Sébastien Guillet, Virginie Poulain, Slimane Bekki, Joël Guiot, Brian H. Luckman, Clive Oppenheimer, Martin Beniston and Valérie Masson-Delmotte

Nature Geoscience **8,** 784–788 (2015)

The original version of this file referred to a linear scaling of AOD(peak) = 0.02 $M^{0.658}$, which was then compared to the results of this work. This scaling has been corrected to AOD = Loading (in grams) / 1.5×10^{14}. In addition, the scaling should have been attributed to Gao *et al.* 2008, instead of Gao *et al.* 2007. Finally, a reference to Arfeuille *et al.* 2014 should have been given, which has now been added.

nature geoscience

SUPPLEMENTARY INFORMATION

DOI: 10.1038/NGEO2526

Estimates of volcanic-induced cooling in the Northern Hemisphere over the past 1,500 years

Markus Stoffel, Myriam Khodri, Christophe Corona, Sébastien Guillet, Virginie Poulain, Slimane Bekki, Joël Guiot, Brian H. Luckman, Clive Oppenheimer, Martin Beniston, Valérie Masson-Delmotte

Correspondence to markus.stoffel@dendrolab.ch

Structure and content of the Supplementary Information

Table S1. Tree-ring chronologies used in this study for the reconstruction of Northern hemisphere (NH) JJA temperature anomalies for the period 500–2003. The 30 clusters are composed of 233 site chronologies comprising 10,078 tree-ring series.

Figure S1. Overview of the tree-ring width (TRW) and maximum latewood density (MXD) chronologies used for reconstruction: (a) Location of the 30 MXD and TRW temperature-sensitive clusters used in this study for the reconstruction of NH JJA temperature. (b) Colour code for the length of chronologies and periods covered.

Note A. Additional explanation for Tables S2 and S3.

Table S2. Statistics of reconstructed JJA temperature in NH1 reconstruction (calibrated against BEST dataset) for each nest.

Table S3. Statistics of reconstructed JJA temperature in NH2 for each cluster.

Table S4. Rank of identified volcanic cooling in NH1 and NH2.

Figure S2. Dendroclimatic reconstruction of NH (40–90°N) JJA anomalies (wrt 1961–1990) based on the nested approach and using exclusively tree-ring width (TRW) chronologies. (a) sample size, (b) statistics of the reconstruction, (c) TRW reconstruction based on 27 nested models and calibrated against instrumental JJA temperatures averaged over the NH, (d) comparison of TRW reconstruction with NH1 for the five largest eruptions of the last millennium.

Figure S3. Comparison between NH1/NH2 and (a) last Millennium Paleoclimate Model Intercomparison Project (PMIP3) simulations, (b) upper (US) and lower (LS) scenarios SC1 (53.2 Tg SO_2) and (c) SC3 (137.8 Tg SO_2) for the 1257 Samalas eruption with injections starting either in May or July 1257 and January 1258. Upper (US) and lower (LS) scenarios (d) SC4 (30.0 Tg SO_2), (e) SC6 (83.6 Tg SO_2) for the 1815 Tambora eruption with injections starting in April 1815.

Table S5. Overview of PMIP3 / CMIP5 Last Millennium simulations as well as solar and volcanic forcings used in this study.

Note B. Additional methodology – Numerical simulations

Figure S4. Location of Antarctic and Greenland ice core sites used to estimate SO_2 deposition for the 1257 Samalas and AD 1815 Tambora events. The black letters refer to ice cores in common with GAO07, GAO08 and CR12; the black letters with asterisk correspond to ice cores used in GAO07, GAO08 and CR12 and which estimated values were updated (see Tables S6a-b and S7a-b); the red letters refer to ice cores not included in GAO07, GAO8 and CR12.

Figure S5. (a) Pattern of annual precipitation over Greenland from Box et al. (2004) and (b) long-term accumulation distribution from Bromwich et al. (2004).

Figure S6. Probability density function of Greenland and Antarctic sulphate deposition (kg km^{-2}) obtained for each eruption using a random regional weighting of ice cores

Table S6a. List of Antarctic ice cores used to estimate sulphate flux for Samalas eruption along with corresponding references. Capital letters, in the left column refer to symbols used to locate each ice core site on Figure S4. Bold letters indicate ice cores not used in previous datasets: GAO07, GAO08 and CR12.

Table S6b. List of Greenland ice cores used to estimate sulphate flux for Samalas eruption along with corresponding references. Capital letters, in the left column, refer to symbols used to locate each ice core site on Figure S4. Bold letters indicate ice cores not used in previous datasets: GAO07, GAO08 and CR12.

Table S7a. List of Antarctic ice cores used to estimate sulfate flux for the Tambora eruption along with corresponding references. Capital letters, in the left column, refer to symbols used to locate each ice core site on Figure S4. Bold letters indicate ice cores not used in previous datasets: GAO07, GAO08 and CR12.. Italicized letters indicate ice cores for which values were updated from those used in GAO07, GAO08.

Table S7b. List of Greenland ice cores used to estimate sulfate flux for the Tambora eruption along with corresponding references. Capital letters, in the left column, refer to symbols used to locate each ice core site on

Figure S4. Bold letters indicate ice cores not used in previous datasets: GAO07, GAO08 and CR12.. Italicized letters indicate ice cores for which values were updated from those used in GAO07, GAO08.

Table S8: Ice core estimates of hemispheric and total sulphate deposition (kg km^{-2}) for Samalas and Tambora eruptions.

Table S9. Mean values and variances obtained using simple hemispheric average (μ0), climatological regional weighting taking into account the regional climatological accumulation rates (μ1) and with a random regional averaging of ice cores (μ2) repeated a thousand times to build a probability density function for each hemisphere. The asterisk (*) next to listed mean values indicates that the null hypothesis (μ0 = μ1) is accepted based on a Student test.

Table S10. Total SO_2 injected (Tg), altitude of injection and month of injection for Samalas and Tambora eruptions.

Table S11. Statistics of reconstructed JJA temperature in alternative NH1 reconstruction (calibrated against CRUTEM4 dataset, 1880-1976) for each nest.

Figure S7. Modelled stratospheric AOD using the (a-b-c) maximum (SC3), (d-e-f) mean (SC2) and (g-h-i) minimum (SC1) scenario of SO_2 loading for Samalas in January (left), May (right) and July (middle) for the lower injection (LS) scenario.

Figure S8. Same as in Figure S7 for Samalas but for the upper injection scenario (US).

Figure S9. Modelled stratospheric AOD using the (a) maximum (SC6), (b) mean (SC5) and (c) minimum (SC4) scenario of SO_2 loading for Tambora eruption in April for the upper injection (US) scenario. The lower injection (LS) scenarios are shown on the lower panels (d-f).

Figure S10. Reconstructed aerosol optical depth (AOD) from Gao et al. (2008) on the left, and from Crowley and Unterman (2013) on the right, for Mt Pinatubo (June 1991), Tambora (April 1815) and Salamas. The Samalas eruption starts in April 1258 in Gao et al. (2008), while the eruption starts in September 1257 in Crowley and Unterman (2013).

Figure S11. Comparisons between probability density functions (PDFs) from (i) NH1/NH2 reconstructions (red and green), (ii) two millennium-long coupled ocean-atmosphere simulations for either constant pre-industrial condition (PiControl; light blue) or last millennium known forcings (IPSL past1000, P1000; black) and (iii) reconstructed (NH1, NH2) and (iv) simulated (five JJA temperatures sampled randomly) summer cooling induced by the 1257 Samalas eruption with injections starting either in (a) May or July 1257 or (b) January 1258 and (c) by the 1815 Tambora eruption.

Figure S12. Alternative tree-ring reconstructions of Northern hemisphere (40–90°N) JJA temperature anomalies since 500 and wrt 1961–1990. Reconstruction is composed of 30 clusters; (a) sample size, (b) statistics of the reconstructions, (c) the reconstruction is based on 32 nested models and calibrated against instrumental JJA temperatures extracted from the CRUTEM4 gridded dataset (1880-1976). The dark green line represents the reconstructed temperature values, the red curves show the 30-yr smoothing. The envelope in pale green illustrates the 95% confidence interval obtained with the bootstrap approach using 1000 iterations. (d) Comparison of alternative reconstruction with NH1 for the five largest eruptions of the last millennium.

Data S1. Evidence for a dry fog in late 1257 in England.

References

Id	Clusters	Latitude	Longitude	No. Sites	No. Sites AD 1200	No. Sites AD 1000	No. Sites AD 800	No. Sites AD 500	No. Series	Parameter	EPS > 0.85	Standardisation	Source
1	Aktash Valley	49°-52°	84°-88°	9	0	0	0	0	183	MXD (a)	1581-1994	ARGC*	*Schweingruber, ITRDB*
2	Ary-Ongorbynh River	66°-72°	111°-123°	6	0	0	0	0	127	MXD	1535-1991	Neg. Exp.**	*Schweingruber, ITRDB*
3	Athabasca	51°-53°	-116°-118°	6	3	3	2	0	101	MXD+TRW	950-1994	RCS***	*Luckman and Wilson, 2005*
4	Calimani Mountains	47°	25°3	1	1	1	0	0	410	TRW (b)	1163-2005	RCS	*Popa and Kern, 2009*
5	Churchill	58°-59°	-95°-93°	2	0	0	0	0	43	MXD	1775-1987	ARGC	*Schweingruber, ITRDB*
6	Coastal Alaska	55°-62°	-154°-131°	22	2	2	2	0	820	TRW	713-2000	RCS	*D'Arrigo et al., 2006; Wilson et al., 2007*
7	Firth River	68°39	-141°38	1	1	1	0	0	246	MXD	1098-2002	SF****	*Anchukaitis et al., 2012*
8	French Alps LADE	44°-46°	6°-7°	41	4	4	3	0	1025	TRW	810-2009	Neg. Exp.	*Corona et al., 2010, 2011*
9	Indigirka	70°	148°	1	1	1	1	1	NA	TRW	500-1993	RCS	*Sidorova and Naurzbaev, 2002*
10	Jämtland	62°-65°	10°-17°	4	1	0	0	0	338	MXD	1235-1978	ARGC	*Schweingruber, ITRDB*
11	Kola Peninsula	64°-70°	29°-33°	3	0	0	0	0	66	MXD	1578-1992	Neg. Exp.	*Schweingruber, ITRDB*
12	Labrador	55°-58°	-63°-61°	9	0	0	0	0	323	TRW	1670-2001	ARGC	*D'Arrigo, Buckley, Jacoby, ITRDB*
13	Lac Romanel	54°-55°	-78°-67°	7	0	0	0	0	208	MXD	1410-1989	ARGC	*Schweingruber, ITRDB*
14	Nscan	66°-70°	19°-29°	17	11	11	11	9	587	MXD	-2144	ARGC	*Esper et al, 2012a, 2012b*
15	Polar Ural	65°-70°	65°-85°	14	1	1	1	0	487	MXD	880-2006	Neg. Exp.	*Briffa et al., 2013*
16	Pyrenees	42°-43°	1°-2°	2	1	0	0	0	46	MXD	1111-1976	Neg. Exp.	*Buntgen et al., 2008; Esper et al., 2013*
17	Qilian Mounains HY	38°-39°	99°-100°	4	4	3	3	0	82	TRW	670-2012	Neg. Exp.	*Zhang et al., unpublished*
18	Sarejmek	41°-43°	75°-79°	4	0	0	0	0	107	MXD	1626-1995	ARGC	*Schweingruber, ITRDB*
19	Sartan River	64°-72°	127°-155°	11	0	0	0	0	289	MXD	1495-1991	ARGC	*Schweingruber, ITRDB*
20	Seward Peninsula	65°-68°	-162°-157°	16	2	0	0	0	1196	TRW	1140-2002	ARGC	*D'Arrigo et al., 2005, 2006*
21	Solongotyn Davaa	47°-49°	97°-100°	1	1	1	0	0	90	TRW	913-1999	ARGC	*D'Arrigo et al., 2001, 2006*
22	STREC Quebec	53°-55°	-70°-73°	6	6	6	6	0	1782	TRW	910-2011	RCS	*Gennaretti et al., 2014*
23	Swiss Alps	46°-47°	7°-11°	4	2	2	2	0	180	MXD	755-2004	RCS	*Buntgen et al., 2006*
24	Tatra Mountains	48°-53°	18°-23°	8	1	0	0	0	545	TRW	1170-2011	ARGC	*Buntgen et al., 2013*
25	Taymir	67°-73°	88°-105°	9	1	1	1	1	501	TRW	-2103	ARGC	*Naurzbaev et al., 2002; Briffa et al., 2008*
26	Thelon	64°-68°	-116°-103°	4	1	0	0	0	706	TRW	1175-2004	ARGC	*D'Arrigo et al., 2006*
27	Torneträsk	68°-69°	19°-20°	1	1	1	1	0	124	MXD	675-2010	ARGC	*Melvin et al., 2012*
28	Vikran	68°-70°	15-19°	4	1	1	1	0	197	TRW	1230-1997	ARGC	*Kirchhefer et al., 2000*
29	Yamal	66°-68°	69°-70°	1	1	1	1	1	615	TRW	-2690	SF	*Briffa et al., 2013*
30	Zolotica	59°-67°	41°-61°	15	0	0	0	0	243	MXD	1695-1991	ARGC	*Schweingruber, ITRDB*

Table S1. Tree-ring chronologies used in this study for the reconstruction of Northern hemisphere (NH) JJA temperature anomalies for the period 500–2003. The 30 clusters are composed of 233 site chronologies comprising 10,078 tree-ring series.

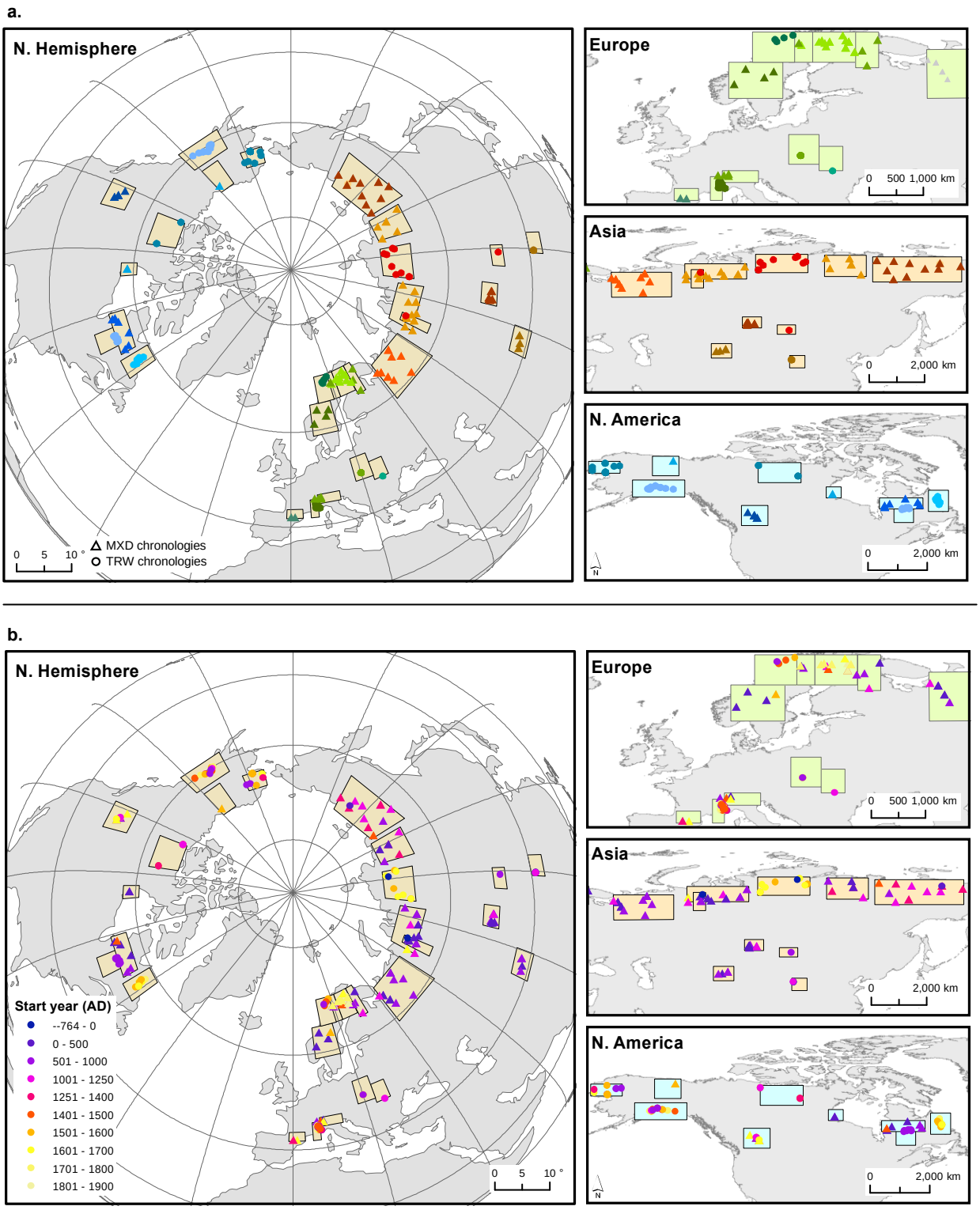

Figure S1. Overview of the tree-ring width (TRW) and maximum latewood density (MXD) chronologies used for reconstruction: (a) Location of the 30 MXD and TRW temperature-sensitive clusters used in this study for the reconstruction of NH JJA temperature. (b) Colour code for the length of chronologies and periods covered.

Note A. Additional explanation for Tables S2 and S3.

Standard calibration and verification statistics typically employed to validate dendroclimatic reconstructions - coefficient of determination (R^2 r^2), reduction of error (RE), coefficient of efficiency (CE) - were calculated to assess the quality and robustness of the reconstructions.

The R^2 (r^2) statistic, which ranges from 0.0 to 1.0, measures the proportion of variance reconstructed over the calibration (verification) period (Cook et al., 1999). The reduction of error (RE) and the coefficient of Efficiency (CE), which range between $-\infty$ and 1.0, measure the proportion of variance reconstructed over the verification period, using as reference the average respectively on the calibration period or the verification period (Cook et al., 1999).

The RE statistic was originally derived by Edward Lorenz (1959) as a test of meteorological forecast skill. It is used to determine if temperature data predicted from the model is closer to the observations than the mean of the calibration period. Therefore, if this statistic is greater than zero, the reconstruction has greater skill than would be obtained by simply using the mean of the calibration period as the value for each year of the reconstruction. A negative RE is generally interpreted as meaning that the estimates are worse than the calibration period mean. It means that the model has no predictive skill.

The main difference between CE and RE is that CE compares the estimates with the mean of the verification period. CE is never greater than RE and is often significantly smaller. A positive value indicates that the model has better predictive skill than simply using the overall mean of the verification period. p is the number of principal components used in each nested model.

Nest Period	500-670	670-675	675-713	713-755	755-810	810-880	880-913	913-950	950-1098
N Chronologies	4	5	6	7	8	9	10	12	13
p	3	4	4	4	7	3	4	4	7
R2b	0.25[0.14-0.37]	0.25[0.15-0.39]	0.26[0.15-0.37]	0.26[0.16-0.37]	0.36[0.24-0.49]	0.32[0.21-0.42]	0.34[0.21-0.48]	0.34[0.23-0.5]	0.38[0.26-0.52]
r2b	0.19[-0.09-0.34]	0.23[-0.16-0.32]	0.21[-0.05-0.32]	0.21[-0.01-0.35]	0.27[-0.12-0.43]	0.28[-0.02-0.41]	0.3[-0.08-0.44]	0.3[0.04-0.47]	0.3[-0.17-0.43]
REb	0.2[-0.07-0.34]	0.23[-0.09-0.32]	0.21[-0.02-0.32]	0.22[-0.02-0.34]	0.28[-0.09-0.42]	0.29[0.02-0.42]	0.29[0.07-0.43]	0.31[0.12-0.48]	0.3[-0.14-0.43]
CEb	0.18[-0.11-0.32]	0.21[-0.18-0.31]	0.2[-0.07-0.31]	0.2[-0.03-0.34]	0.26[-0.13-0.42]	0.27[-0.04-0.4]	0.28[-0.1-0.43]	0.29[0.02-0.46]	0.29[-0.19-0.43]

Nest Period	1098-1111	1111-1140	1140-1163	1163-1170	1170-1175	1175-1230	1230-1235	1235-1410	1410-1495
N Chronologies	14	15	16	17	18	19	20	21	22
p	4	3	3	4	4	5	4	4	5
R2b	0.36[0.25-0.47]	0.37[0.25-0.48]	0.37[0.26-0.47]	0.39[0.25-0.51]	0.39[0.28-0.52]	0.39[0.27-0.53]	0.41[0.28-0.54]	0.39[0.25-0.53]	0.44[0.33-0.57]
r2b	0.31[0.03-0.43]	0.31[-0.09-0.48]	0.35[-0.02-0.48]	0.33[0.02-0.46]	0.33[-0.04-0.46]	0.34[-0.04-0.5]	0.34[-0.02-0.45]	0.36[0.08-0.47]	0.4[0.02-0.55]
REb	0.33[0.06-0.43]	0.33[0.02-0.47]	0.35[0.02-0.48]	0.34[0.05-0.46]	0.34[-0.03-0.45]	0.35[-0.02-0.5]	0.35[0.01-0.44]	0.35[0.07-0.47]	0.4[0.07-0.54]
CEb	0.3[0.02-0.43]	0.3[-0.11-0.47]	0.34[-0.04-0.48]	0.31[0-0.46]	0.32[-0.05-0.45]	0.33[-0.06-0.49]	0.33[-0.04-0.44]	0.34[0.06-0.46]	0.39[0-0.54]

Nest Period	1495-1535	1535-1578	1578-1581	1581-1626	1626-1670	1670-1695	1695-1775	1775-1976	1976-1988
N Chronologies	23	24	25	26	27	28	29	30	28
p	6	7	9	5	9	4	4	6	4
R2b	0.46[0.33-0.6]	0.48[0.33-0.6]	0.5[0.37-0.61]	0.44[0.33-0.58]	0.5[0.36-0.63]	0.43[0.33-0.56]	0.49[0.36-0.59]	0.51[0.37-0.64]	0.5[0.36-0.62]
r2b	0.41[-0.06-0.55]	0.39[-0.18-0.55]	0.4[0.01-0.56]	0.42[0.08-0.57]	0.4[0.12-0.59]	0.39[0.14-0.55]	0.42[0.02-0.54]	0.45[0.09-0.61]	0.45[0.18-0.61]
REb	0.41[0.09-0.54]	0.4[-0.1-0.55]	0.41[0.08-0.56]	0.42[0.1-0.57]	0.42[0.11-0.59]	0.39[0.14-0.54]	0.42[0.07-0.55]	0.47[0.2-0.61]	0.46[0.23-0.61]
CEb	0.4[-0.08-0.54]	0.38[-0.2-0.54]	0.39[0-0.55]	0.41[0.06-0.56]	0.39[0.1-0.58]	0.38[0.13-0.54]	0.41[0-0.54]	0.44[0.07-0.6]	0.45[0.17-0.61]

Nest Period	1988-1991	1991-1994	1994-1997	1997-2001	2001-2003
N Chronologies	26	21	18	16	12
p	5	5	5	5	3
R2b	0.41[0.31-0.54]	0.38[0.26-0.51]	0.36[0.26-0.5]	0.37[0.25-0.51]	0.39[0.22-0.52]
r2b	0.37[0.09-0.51]	0.33[-0.29-0.44]	0.32[-0.06-0.45]	0.34[-0.02-0.45]	0.33[-0.14-0.51]
REb	0.39[0.08-0.51]	0.33[-0.17-0.44]	0.32[-0.01-0.46]	0.34[0.01-0.46]	0.34[-0.16-0.5]
CEb	0.36[0.07-0.5]	0.32[-0.31-0.43]	0.31[-0.08-0.44]	0.32[-0.03-0.44]	0.32[-0.16-0.5]

N Chronologies : Number of chronologies
p : Number of principal components
Median value of R2b (1000 bootstrap iterations) calculated over the calibration period
Median value of r2b (1000 bootstrap iterations) calculated over the validation period
Median value of REb : Reduction of error (1000 bootstrap iterations)
Median value of CEb : Coefficient of efficiency (1000 bootstrap iterations)
Numbers in brackets refer to the 2.5th and 97.5th percentiles of the R2,r2,RE,CE distributions

Table S2. Statistics of reconstructed JJA temperature in NH1 reconstruction (calibrated against BEST dataset) for each nest.

Clusters	Instrumental Data	Calibration Period	Calibration Season	R2 (1901-1990)	RE (1901-1945)	RE (1946-1990)	CE (1901-1945)	CE (1946-1990)	Comments
Aktash Valley	CRU	1901-1990	JJA	0.52	0.42	0.62	0.42	0.61	Cluster included in the NH2 reconstruction
Ary-Ongorbynf River	BEST	1901-1990	JJA	0.42	0.45	0.33	0.45	0.32	Cluster included in the NH2 reconstruction
Athabasca	BEST	1901-1990	JJA	0.32	0.12	0.31	0.04	0.26	Cluster included in the NH2 reconstruction
Calimani mountains	BEST	1901-1990	JJA	NA	NA	NA	NA	NA	Cluster included in the NH2 reconstruction
China	*BEST*	*1901-1990*	*JJA*	*0.05*	*0.44*	*-0.76*	*-0.47*	*-0.78*	*Weak correlations with JJA temperatures, not included in the NH2 reconstruction*
Churchill	BEST	1901-1987	JJA	0.43	0.13	0.39	0.12	0.38	Cluster included in the NH2 reconstruction
Coastal Alaska	*NA*	*NA*	*NA*	*NA*	*NA*	*NA*	*NA*	*NA*	*Weak correlations with JJA temperatures, not included in the NH2 reconstruction*
Firth River	BEST	1901-1990	JJA	0.35	0.36	0.33	0.35	0.32	Cluster included in the NH2 reconstruction
French Alps LADE	BEST	1901-1990	JJA	0.19	0.19	0.16	0.17	0.15	Cluster included in the NH2 reconstruction
Indigirka	*CRU*	*1901-1990*	*JJA*	*0.16*	*-0.52*	*0.14*	*-0.58*	*0.12*	*Weak correlations with JJA temperatures, not included in the NH2 reconstruction*
Jämtland	BEST	1901-1978	JJA	0.65	0.65	0.27	0.65	0.25	Cluster included in the NH2 reconstruction
Kola Peninsula	CRU	1901-1990	JJA	0.45	0.38	0.26	0.36	0.23	Cluster included in the NH2 reconstruction
Labrador	BEST	1901-1990	JJA	0.21	0.24	0.31	0.04	0.14	Cluster included in the NH2 reconstruction
Lac Romanel	BEST	1901-1989	JJA	0.38	0.20	0.31	0.15	0.27	Cluster included in the NH2 reconstruction
Nscan	CRU	1901-1990	JJA	0.55	0.41	0.40	0.41	0.39	Cluster included in the NH2 reconstruction
Polar Ural	CRU	1901-1990	JJA	0.74	0.72	0.63	0.72	0.63	Cluster included in the NH2 reconstruction
Pyrenees	CRU	1901-1976	JJA	NA	NA	NA	NA	NA	Cluster included in the NH2 reconstruction
Sarejmek	CRU	1901-1990	JJA	0.33	0.25	0.27	0.16	0.15	Cluster included in the NH2 reconstruction
Sartan River	BEST	1901-1990	JJA	0.4	0.13	0.30	0.11	0.28	Cluster included in the NH2 reconstruction
Seward Peninsula	*BEST*	*1901-1990*	*JJA*	*0.10*	*0.13*	*0.01*	*0.07*	*-0.05*	*Weak correlations with JJA temperatures, not included in the NH2 reconstruction*
Solongotyn Davaa	*BEST*	*1901-1990*	*JJA*	*0.12*	*0.01*	*0.26*	*-0.63*	*-0.25*	*Weak correlations with JJA temperatures, not included in the NH2 reconstruction*
STREC Quebec	*CRU*	*1901-1990*	*JJA*	*0.36*	*0.52*	*0.44*	*0.28*	*-0.07*	*Weak correlations with JJA temperatures, not included in the NH2 reconstruction*
Swiss Alps	BEST	1901-1990	JJA	0.43	0.35	0.25	0.33	0.23	Cluster included in the NH2 reconstruction
Tatra Mountains	*BEST*	*1901-1990*	*JJA*	*0.07*	*0.11*	*0.07*	*-0.15*	*-0.26*	*Weak correlations with JJA temperatures, not included in the NH2 reconstruction*
Taymir	BEST	1901-1990	JJA	0.26	0.27	0.23	0.26	0.23	Cluster included in the NH2 reconstruction
Thelon - Coppermine	*BEST*	*1901-1990*	*JJA*	*0.13*	*-0.09*	*0.10*	*-0.09*	*0.10*	*Weak correlations with JJA temperatures, not included in the NH2 reconstruction*
Torneträsk	CRU	1901-1990	JJA	0.65	0.60	0.60	0.58	0.59	Cluster included in the NH2 reconstruction
Vikran	CRU	1901-1990	JJA	0.38	0.42	0.29	0.40	0.26	Cluster included in the NH2 reconstruction
Yamal	BEST	1901-1990	JJA	0.27	0.21	0.31	0.20	0.30	Cluster included in the NH2 reconstruction
Zolotica	CRU	1901-1990	JJA	0.48	0.22	0.38	0.21	0.38	Cluster included in the NH2 reconstruction

Table S3. Statistics of reconstructed JJA temperature in NH2 for each cluster.

Rank	Years	JJA Temperature wrt 1961-1990	Volcanic eruptions	References
1	**1453**	**-1.78**	**Kuwae, Vanuatu?**	**Briffa et al, 1998; Witter and Self, 2007; Plummer et al., 2012; Cole-Dai et al., 2013**
2	**1816**	**-1.57**	**Tambora, Indonesia**	**Stothers, 1984; Oppenheimer, 2003b**
3	**536**	**-1.56**	**Ilopango, El Salvador?**	**Stothers, 1984; Dull et al., 2010**
4	**1601**	**-1.39**	**Huaynaputina, Peru**	**Briffa et al, 1998;**
5	**1783**	**-1.36**	**Laki, Iceland**	**Thordarsson et al., 2003**
6	**1642**	**-1.31**	**Parker, Philippines**	**Briffa et al, 1998**
7	**1259**	**-1.31**	**Samalas, Indonesia**	**Lavigne et al., 2013**
8	**1817**	**-1.29**	**Tambora, Indonesia**	**Stothers, 1984; Oppenheimer, 2003b**
9	1593	-1.27		
10	**1641**	**-1.20**	**Parker, Philippines**	**Briffa et al, 1998**
11	**1258**	**-1.18**	**Samalas, Indonesia**	**Lavigne et al., 2013**
12	1466	-1.17		
13	**1032**	**-1.15**	**Unknown event**	**Oppenheimer, 2003a**
14	**541**	**-1.13**	**Volcanic eruption?**	**Baillie, 1994; Baillie, 2008**
15	1695	-1.11		
16	1580	-1.07		
17	**1836**	**-1.06**	**Coseguina, Nicaragua?**	**Briffa et al, 1998**
18	1585	-1.02		
19	1698	-1.01		
20	1109	-1.01		
21	1180	-0.96		
22	546	-0.95		
23	1699	-0.93		
24	800	-0.93		
25	1833	-0.91		
26	537	-0.91		
27	1918	-0.91		
28	**1837**	**-0.9**	**Coseguina, Nicaragua?**	**Briffa et al, 1998**
29	1004	-0.90		
30	1667	-0.89		

NH2

Rank	Years	JJA Temperature wrt 1961-1990	Volcanic eruptions	References
1	**536**	**-2.07**	**Ilopango, El Salvador?**	**Stothers, 1984; Dull et al., 2010**
2	**1453**	**-1.82**	**Kuwae, Vanuatu?**	**Briffa et al, 1998; Witter and Self, 2007; Plummer et al., 2012; Cole-Dai et al., 2013**
3	800	-1.78		
4	**1601**	**-1.60**	**Huaynaputina, Peru**	**Briffa et al, 1998**
5	543	-1.48		
6	903	-1.47		
7	1109	-1.41		
8	**1816**	**-1.40**	**Tambora, Indonesia**	**Stothers, 1984; Oppenheimer, 2003b**
9	**541**	**-1.39**	**Volcanic eruption?**	**Baillie, 1994; Baillie, 2008**
10	**940**	**-1.38**	**Eldgjá**	**Oman, 2006**
11	627	-1.37		
12	546	-1.31		
13	544	-1.29		
14	**1783**	**-1.27**	**Laki, Iceland**	**Thordarsson et al., 2003**
15	596	-1.27		
16	**1837**	**-1.25**	**Coseguina, Nicaragua?**	**Briffa et al, 1998**
17	**1259**	**-1.23**	**Samalas, Indonesia**	**Lavigne et al., 2013**
18	545	-1.22		
19	814	-1.22		
20	**1817**	**-1.20**	**Tambora, Indonesia**	
21	**1642**	**-1.16**	**Parker, Philippines**	**Briffa et al, 1998**
22	574	-1.15		
23	854	-1.15		
24	639	-1.11		
25	**1258**	**-1.10**	**Samalas, Indonesia**	**Lavigne et al., 2013**
26	1346	-1.09		
27	538	-1.09		
28	1699	-1.09		
29	1263	-1.08		
30	1812	-1.07		

Table S4. Rank of identified volcanic cooling in NH1 and NH2.

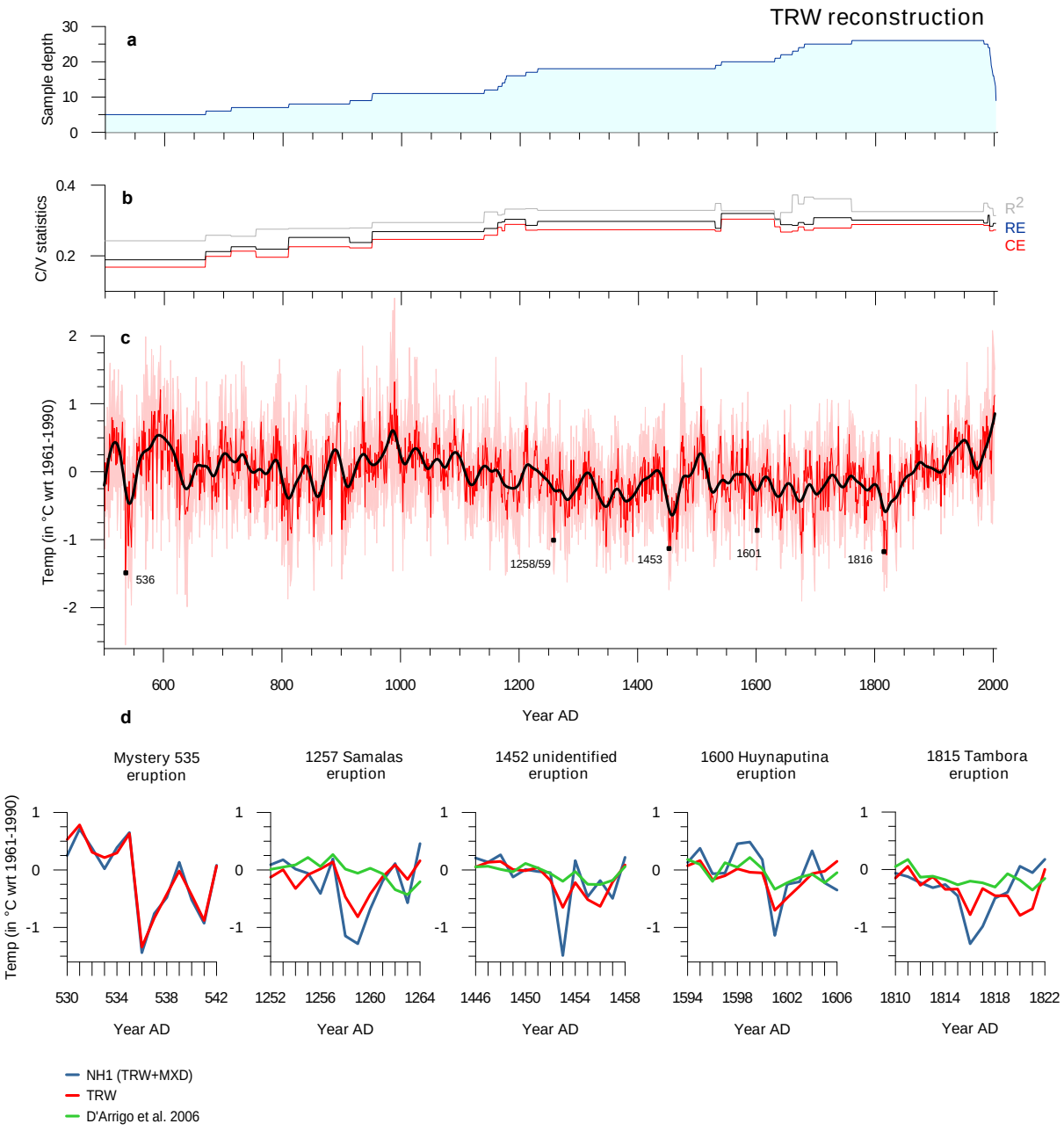

Figure S2. Dendroclimatic reconstruction of NH (40–90°N) JJA anomalies (wrt 1961–1990) based on the nested approach and using exclusively tree-ring width (TRW) chronologies. (a) sample size, (b) statistics of the reconstruction, (c) TRW reconstruction based on 27 nested models and calibrated against instrumental JJA temperatures averaged over the NH, (d) comparison of TRW reconstruction with NH1 for the five largest eruptions of the last millennium.

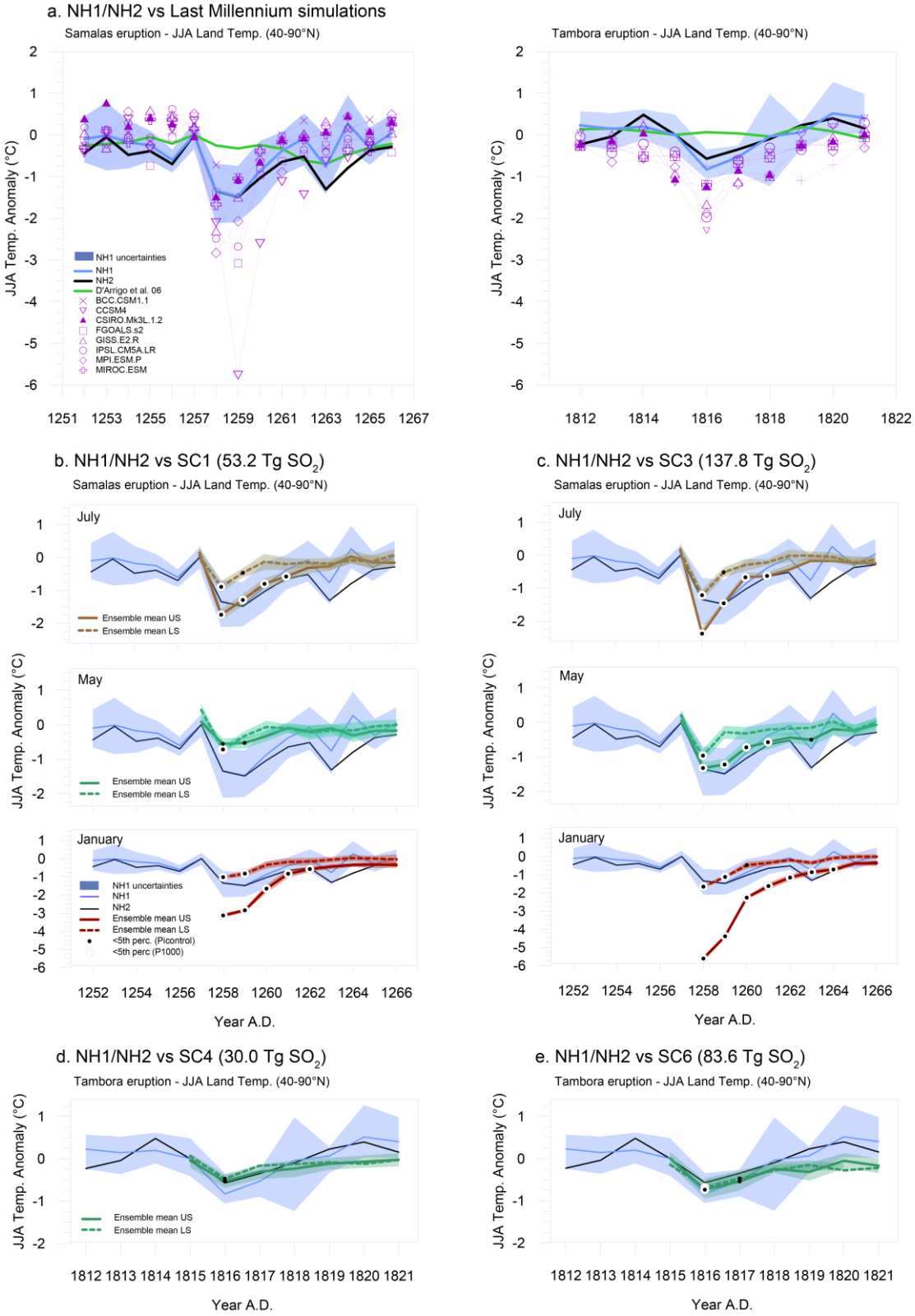

Figure S3. Comparison between NH1/NH2 and (a) last Millennium Paleoclimate Model Intercomparison Project (PMIP3) simulations, (b) upper (US) and lower (LS) scenarios SC1 (53.2 Tg SO_2) and (c) SC3 (137.8 Tg SO_2) for the 1257 Samalas eruption with injections starting either in May or July 1257 and January 1258. Upper (US) and lower (LS) scenarios (d) SC4 (30.0 Tg SO_2), (e) SC6 (83.6 Tg SO_2) for the 1815 Tambora eruption with injections starting in April 1815.

Model	Institute	Model Reference	Transient Volcanic and Solar forcing
IPSL-CM5A-LR	IPSL, France	Dufresne et al., 2013	**Volcanic** Gao et al., 2008; Amman et al., 2007. ***Solar*** *Vieira and Solanki, 2010; Wang et al., 2005.*
CCSM4	NCAR, USA	Gent et al., 2011	**Volcanic** Gao et al., 2008. ***Solar*** *Vieira and Solanki, 2010.*
BCC-CSM1-1	BCC, China	Wu et al., 2013	**Volcanic** Gao et al., 2008. ***Solar*** *Vieira and Solanki, 2010.*
GISS-E2-R	NASA-GISS, USA	Schmidt et al., 2006	**Volcanic** Gao et al., 2008. ***Solar*** *Vieira and Solanki, 2010.*
MIROC-ESM	MIROC, Japan	Watanabe et al., 2010	**Volcanic** Crowley et al., 2008. ***Solar*** *Delaygue and Bard, 2011; Wang et al., 2005.*
MPI-ESM-P	MPI-M, Germany	Marsland et al., 2003; Raddatz et al., 2007	**Volcanic** Gao et al., 2008; Amman et al., 2007. ***Solar*** *Vieira and Solanki, 2010; Wang et al., 2005.*
CSIRO-Mk3L-1-2	UNSW, Australia	Phipps S.J., 2010	**Volcanic** Crowley et al., 2008. ***Solar*** *Steinhilber et al., 2009.*
FGOALS-s2	LASG-IAP, China	Bao et al., 2013	**Volcanic** Gao et al., 2008. ***Solar*** *Vieira and Solanki, 2010.*

Table S5. Overview of PMIP3 / CMIP5 Last Millennium simulations as well as solar and volcanic forcings used in this study.

Note B. Additional methodology – Numerical simulations

- **Samalas and Tambora estimated sulfate deposition from published ice core records**

We used published estimates of volcanic corrected sulfate fluxes deduced from sulfate and sulfur concentration records measured in polar ice cores of both hemispheres. The site locations of Greenland and Antarctic ice cores used in our reconstruction are shown in Figure S4. The flux estimates for each ice core for the Samalas and Tambora eruptions are listed in Tables S6a-b and S7a-b.

In the case of the Samalas eruption, we use a total of 21 published ice cores, of which some are the same as those used by Gao et al. (2007, 2008) (seven ice cores; referred to as GAO07 and GAO08, hereafter) and Crowley and Unterman (2013) (CR12, hereafter). For the Tambora eruption we considered 45 published ice core datasets (of which 27 were used in GAO07 and GAO08, among these 27, we updated 4 ice-core estimates). The range of estimated values for each of the ice cores are summarized in Table S8.

We then estimated the sulfate deposition for the Greenland and Antarctic ice cores separately and evaluated the range of uncertainty. In the case of the closely located Antarctic ice core labelled D (Sigl et al, 2013) and E (Palmer et al, 2004) shown in on Fig. 4, for instance, published estimated fluxes differ from each other by a factor of 3.8 in the case of the Tambora eruption (Table S7a). These considerable differences point to spatial sampling bias, inaccuracies in the flux corrections and re-deposition and wind burst effects at the contemporary ice surface.

In previous work, several methods in spatial averaging have been employed in an attempt to deduce sulphate fluxes from polar ice cores. The methodology described in GAO07, for instance, includes a regional weighting to take account of the spatial heterogeneity of dry deposition and precipitation climatology over Greenland and Antarctica (see Fig. S5a,b). GAO07 also assumed that sulphate aerosols are distributed more or less homogeneously in the atmosphere and that deposition on the ice sheet would depend mostly on accumulation rates (Bromwich et al. 2004; Box et al., 2004).

We tested the methodology described by GAO07 but using our new ice core compilations for each hemisphere and for both the Samalas and Tambora eruptions. Results (μ1) listed in Table S8 were then compared to the mean values and variances obtained with a simple hemispheric averaging (μ0) and with a random regional weighting (μ2) which we repeated 1000 times to build a probability density function for each hemisphere (PDF, Fig. S6). The PDF and the simple global averaging were designed to test the validity of using a regional weighting based on climatological accumulation rates by comparing the mean values obtained for each hemisphere. The three methodologies also enable comparison of mean standard deviations due to a random or global average.

We perform a Student test on simple global average (μ0) and climatological regional weighting (μ1). The null hypothesis corresponds to μ0 = μ1. This test is accepted at the 95% confidence level in all cases, which means that the regionalization used in GAO07 has no statistical effect on the mean of sulphate flux estimates. Both methods provided comparable means (57–59 kg km^{-2} in the case of Tambora and 94–102 kg km^{-2} for Samalas) but much larger standard deviations in the case of simple global average (μ0; see Table S8 for details). We thus conclude that the regionalisation method has an impact on the spread of sulphate deposition, with the method presented in GAO07 yielding a smaller standard deviation, but that the choice does not impact the mean.

To construct our scenarios and to take into consideration the uncertainties of estimated sulphate deposition, we therefore define a “mean scenario” representing the average sulphate deposition over the compiled bipolar ice cores arrays which we name SC2 and SC5 for the Samalas and Tambora eruptions, respectively. In addition, one minimum (SC1 and SC4) and maximum (SC3 and SC6) scenario is defined for the Samalas and Tambora eruptions, respectively, and defined as the mean minus or plus one standard deviation. The approach was defined in a way to take account of the range of uncertainties for each eruption (SC1 to SC6, Tables S8-S9-S10).

- **Stratospheric SO_2 loading**

Next, we convert the sulfate deposition flux to stratospheric SO_2 loading following the methodology described by GAO07. The average sulfate deposition for each hemisphere is multiplied by half of the mean calibration factor ($L_{1/2}$=1 × 10^9 km^2) to derive hemispheric loading. Both loadings are then added to give the global sulfate atmospheric loading which is converted to an SO_2 injection assuming a H_2SO_4 mass fraction of 75%. Table S10 shows the total SO_2 injected for each eruption and for each of the six scenarios (SC1–SC6). The mean scenario (SC5) for Tambora is very similar to GAO07s scenario and also in line with the latest calculations based on geological data as presented by S. Self (Tambora bicentennial conference, April 2015, Bern; *verbatim*), whereas the mean Samalas scenario (SC2) is close to the one presented by CR12 and the maximum Samalas scenario (SC3) is closer to that given by GAO07 (Table S9). The strongest difference with the scenarios used in PMIP arises from the aerosols optical properties that cannot be scaled considering only the underlying SO_2 emissions.

Based on this SO2 loading, Gao et al. (2008) give the relationship between the AOD and aerosol masses following this empirical relationship AOD =Loading (g) / 1.5 x 10^14. This equation is used to derive aerosol optical properties assuming a linear scaling with those observed for Pinatubo. It is obvious from our fully explicit microphysical calculation that one needs to consider not only self-limiting microphysical processes but also the stratospheric circulation, as stressed by other studies (i.e. Arfeuille et al., 2014; Toohey et al, 2011; Timmreck et al, 2009), which affects both the size and spatial distribution of the volcanic aerosol. This is well illustrated by the figure S7- S10 comparing GAO07 and CR12's AOD to that computed by our microphysical model.

- **Chemistry-transport-aerosol global model**

The model used to calculate the time-evolving global distribution of stratospheric volcanic aerosols is a global, two-dimensional (zonally-averaged) chemistry-transport model containing a detailed treatment of stratospheric aerosol microphysics. Its basic formulation is described in Harwood and Pyle (1975) and Law and Pyle (1993). It extends from pole to pole and from the ground to ~60 km with a horizontal resolution of 9.5 degrees and a vertical resolution of half the pressure scale height (~3.5 km). It is mostly a stratospheric model with between 14 to 17 levels in the stratosphere (depending on latitude). It contains detailed representations of atmospheric chemistry (including wet/dry deposition) and transport. The sulphuric acid aerosol microphysics and the photochemical scheme for O_x, NO_x, HO_x, ClO_x, BrO_x, CHO_x, and SO_x are based on the work of Bekki and Pyle (1992). Gas phase reaction rates, photolysis cross-sections and heterogeneous reaction probabilities on sulfuric acid aerosol particles (including volcanic aerosols) follow the Jet Propulsion Laboratory recommendations (Sander et al., 2011).

The mean atmospheric circulation is calculated from forcing terms that include solar heating by O_2 and O_3 and longwave heating in the stratosphere by CO_2, H_2O, O_3, CH_4 and N_2O. Tropospheric heating rates and surface temperatures are specified. The sulfate aerosols are treated as liquid sulphuric acid solution droplets with a size distribution between 0.001 and 4 μm over 38 size bins. The aerosol microphysical module accounts for all the relevant stratospheric aerosol microphysical processes (nucleation, coagulation, condensation/evaporation, gravitational sedimentation, and tropospheric rainout), including evaporation in the upper stratosphere. The model has been extensively used in the climate-chemistry community and validated against a range of Mt Pinatubo eruption observations (Bekki and Pyle, 1994, SPARC, 2006). It has already been used to study the impact of sulfur injections from very large volcanic eruptions on stratospheric aerosol loading and chemical composition (Bekki, 1995; Bekki et al., 1996; Savarino et al., 2003). The surface mixing ratios of the major source gases are here set to values thought to be representative of a pre-industrial atmosphere (CO_2 = 250 ppmv; CH_4 = 400 ppbv; N_2O = 200 pptv; CH_3Cl = 450 pptv and CH_3Br = 5 pptv; Butler et al., 1999). The simulation of volcanic eruptions is initialized by injecting sulfur as SO_2 gas within the stratosphere.

- **Aerosol model simulation experimental setup**

✓ Altitude of injection

The considered altitude of injection for each eruption is summarized in Table S10.

For both the Samalas and Tambora Plinian eruptions, we try to build the most realistic scenarios based on estimated maximum column heights from isopach and pumice fall deposits and considering that most of the sulfur is found below the maximum height. Indeed, for the Mt Pinatubo eruption of 1991, satellite measurements show that the initial volcanic plume reached almost 30 km (McCormick and Veiga, 1992) but that the SO_2 concentration was peaking below this altitude at around 26 km (Read et al., 1993).
For the Tambora eruption, the maximum column height was estimated to be between 33 and 40 km (Sigurdsson and Carrey, 1989; Self et al., 2004) with a maximum mass at 35 km. To be consistent with these reconstructions, SO_2 is injected between 19 and 40 km with 70% of the mass between 26 and 33 km.

According to Lavigne et al. (2013), the Samalas eruption plume height reached an altitude of 43 km, with a minimum at 34 km and a maximum at 52 km. Accordingly, we injected SO_2 in our model at altitudes comprised between 29 and 50 km with 70% of the SO_2 mass being injected between 36 and 43 km.

To address the uncertainties with regards to the altitude of injection and its impact on temperature anomalies, we ran a complementary set of scenarios with 70% of the SO_2 mass between 22 and 26 km, consistent with the Pinatubo eruption altitude of injection (Read et al., 1993).

✓ Latitude of injection

SO_2 is injected at the location of the volcanoes, which is about 8°S for Tambora and Samalas volcanoes. More details can be found in the main text.

✓ Season of the eruption

For the Samalas eruption, the beginning of SO_2 of injection was set to May or July 1257 (according to Lavigne et al., 2013) and January 1258 (Stothers, 2000). In the case of Tambora, only one season was tested with a start of the SO_2 injection set to April 1815 (Stothers et al., 1984; Self et al., 2004).

✓ Deduced aerosol optical depth (AOD)

The modelled stratospheric AOD for the Maximum scenarios of SO_2 loading (SC1 to SC3 in January, July and May for US, SC1 to SC1 January, July and May for LS, and SC4 to SC6 in April for US and LS) are shown in Fig. S7, S8 and S9. For comparison, we also show in Fig. S10 the reconstructed AOD provided by GAO08 and CR12 for the Samalas, Tambora and Mt Pinatubo (June 1991) eruptions. In GAO08 and CR12, the global distributions of AOD were reconstructed following a scaling of the Mt Pinatubo observed distribution. Figure S7 to S9 clearly shows the strong dependence of the aerosol dispersion on the altitude and the season of the eruption due to the intrinsic altitude- and season-dependent stratosphere dynamics. The explicit modeling of the aerosol cloud formation and evolution within the stratosphere indicates some limitations in the aerosol reconstruction approach based on a linear scaling between Mt Pinatubo AOD and sulfate flux measured in ice core (Poulain et al., submitted).

- **IPSL-CM5A-LR climate model simulations forced by model-calculated volcanic forcings for Samalas and Tambora**

The model-calculated time-varying zonal mean distribution of stratospheric aerosol optical parameters were implemented in the IPSL-CM5A-LR climate model (Dufresne, J.-L. *et al., 2013)* used in the PMIP3 LM exercise. For both the Samalas and Tambora eruptions, an ensemble of ten climate simulations of 10 years duration were branched off in December 1252, 1253, 1254, 1255, and 1256 as well as in December 1799, 1801, 1803, 1805, and 1814 from the IPSL-CM5A-LR LM simulation. These restart dates were chosen by selecting five initial states starting either at a negative or positive ENSO phase based on a Niño 3 index and ensuring that at least five years passed after any other eruptions. We hope that by averaging the 10 members ensemble we will cancel out any bias toward a positive or negative ENSO phase and increase the signal to noise ratio.

For each ensemble, the only other difference with the 1257–1266 and 1815–1822 portions of the IPSL LM simulation corresponds to the aerosol distribution and optical properties implemented in the climate model. In addition we use 2 statistical constrains to measure the signal to noise ratio and evaluate the significance of our simulated temperature anomalies as compared to the probability of these anomalies being the result of purely random internal coupled ocean atmosphere interactions.
The first statistical calculations measure the spread of each ensemble members respectively to the ensemble mean considering the Welch two tailed student-test and taking into account the size of the ensemble such as:

$$t = \frac{\overline{X}_1 - \overline{X}_2}{\sqrt{\frac{s_1^2}{N_1} + \frac{s_2^2}{N_2}}}$$

With N1=N2=10.
We also measure the probability that these anomalies would occur just by chance using a Monte Carlo procedure (cf Figure S11). To do so we repeated a random sampling (1000 times) of JJA Northern Hemisphere Temperature Anomalies (40°N-90°N to be consistent with the tree ring reconstruction) from two millennial long coupled ocean-atmosphere simulations either under constant pre industrial condition (PiControl) or last millennium known forcings (IPSL past1000) simulations. By doing so we obtained two probability density functions (PDFs) to which we compared our model simulations results for each eruption scenario. Theoretically, since our ensemble simulations include 10 members we should use a PDF built by averaging 10 JJA temperature anomalies sampled randomly. However we choose to apply an extreme test of significance (>99%) by comparing our ensemble mean anomaly to a PDF built by sampling randomly only five JJA temperature anomalies at a time. The results are shown Fig. S11.

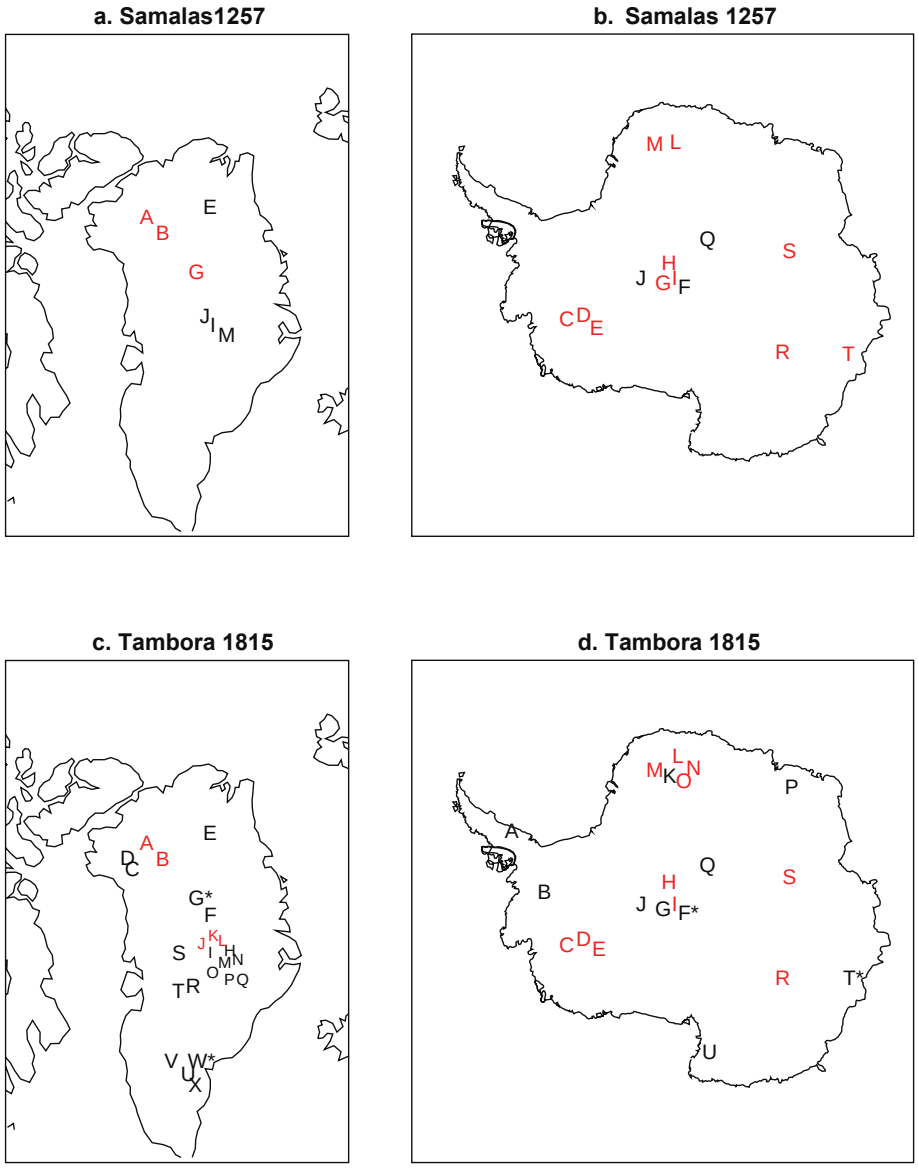

Figure S4. Location of Antarctic and Greenland ice core sites used to estimate SO_2 deposition for the 1257 Samalas and AD 1815 Tambora events. The black letters refer to ice cores in common with GAO07, GAO08 and CR12; the black letters with asterisk correspond to ice cores used in GAO07, GAO08 and CR12 and which estimated values were updated (see Tables S6a-b and S7a-b); the red letters refer to ice cores not included in GAO07, GAO8 and CR12. In the Northern Hemisphere the letters refer to ice core: A Humboldt, B NEEM-2001-S1, C camp century, D GITS, E NGT_B20, F north central, G NGRIP1, H CsiteE, I GISP2, J GRIP1, K summit, L Greenland Site T, M Crete, N CsiteG, O CsiteD, P CsiteB, Q CsiteA, R D3, S D2, T raven, U 18C, V4B, W Dye3, X 20 D. In Southern Hemisphere the letters correspond to the ice core: A Dyer, Siple Station, C WDC06A, D WDC05, E Byrd, F PS1, G SP95, H SP04, I SP84, J SP2001c1, K DMLS_B32, L DML05, M DML07, N DML17, O DML03, P G15, Q plateau remote, R EDC96, S DT401, T Law Dome, U Hercules névé.

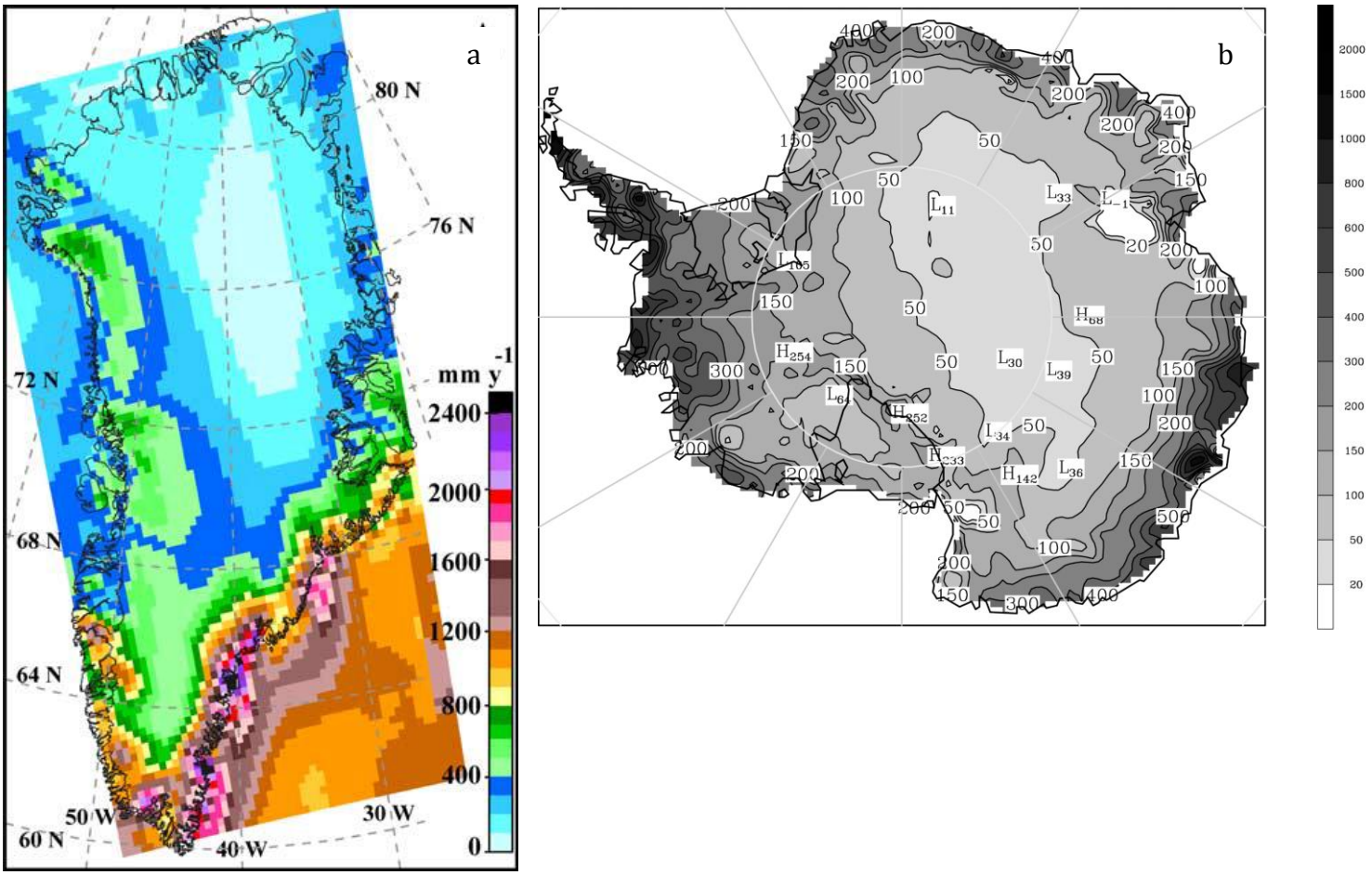

Figure S5. (a) Pattern of annual precipitation over Greenland from Box et al. (2004) and (b) long-term accumulation distribution from Bromwich et al. (2004).

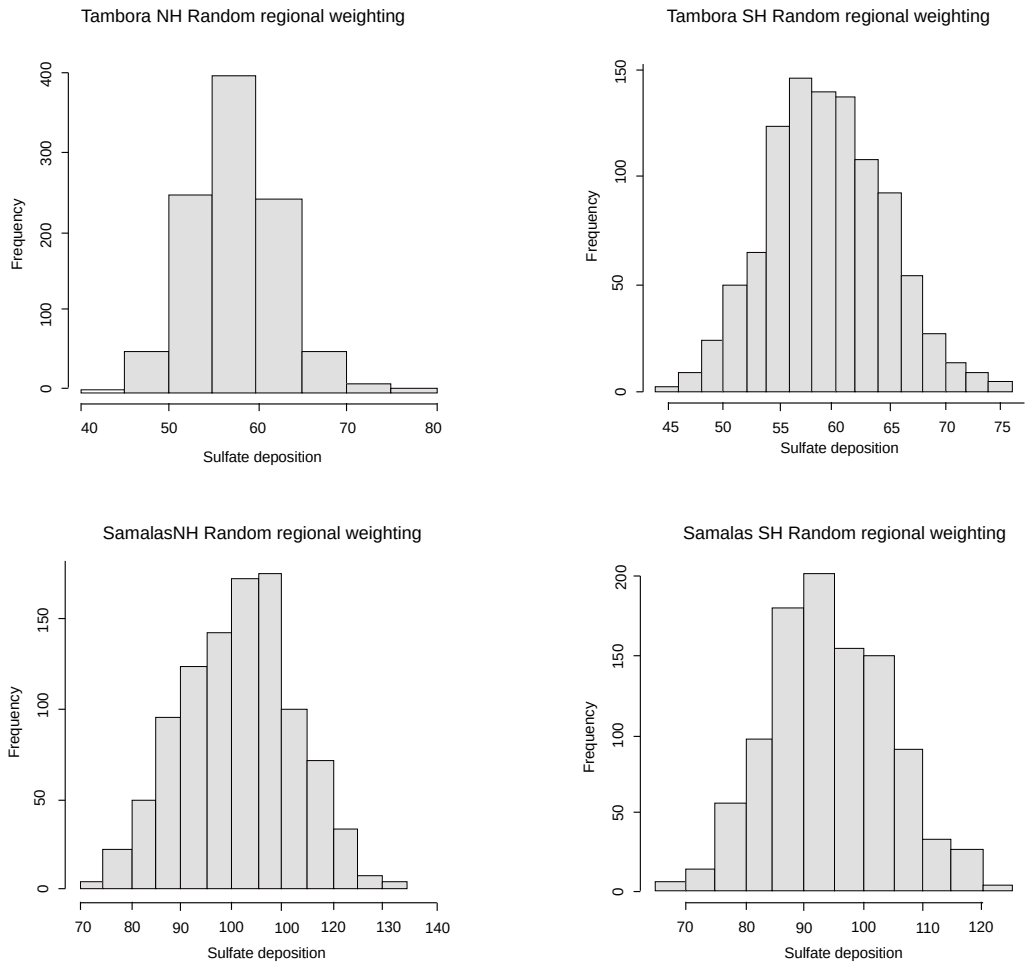

Figure S6. Probability density function of Greenland and Antarctic sulphate deposition (kg km^{-2}) obtained for each eruption using a random regional weighting of ice cores

	Name	Sulfate deposition	Reference
C	**WDC06A**	**99.3**	**Sigl et al., 2013**
D	**WDC05**	**79.7**	**Sigl et al., 2013**
E	**Byrd**	**54**	**Langway et al., 1994**
F	PS1	179.5	Delmas et al., 1992
G	**SP95**	**90**	**Langway et al., 1988**
H	**SP04**	**99.3**	**Ferris et al., 2011**
I	**SP84**	**135.7**	**Delmas et al., 1992**
J	**SP2001c1**	179.45	**Budner et al., 2003**
L	**DML05**	**74.3**	**Traufetter et al., 2004**
M	**DML07**	**58.5**	**Traufetter et al., 2004**
Q	Plateau Remote	46.3	**Cole-dai et al., 2000**
R	**EDC9§**	**60.4**	**Castellano et al., 2005**
S	**DT401**	**66**	**Ren et al., 2010**
T	**Law Dome**	**103.3**	**Plummer et al., 2012**

Table S6a. List of Antarctic ice cores used to estimate sulphate flux for Samalas eruption along with corresponding references. Capital letters, in the left column refer to symbols used to locate each ice core site on Figure S4. Bold letters indicate ice cores not used in previous datasets: GAO07, GAO08 and CR12.

	Name	Sulfate deposition	Reference
A	**Humboldt**	**70**	**Sigl et al., 2013**
B	**NEEM-2011-S1**	**82.1**	**Sigl et al., 2013**
E	NGT_B20	41	Bigler et al., 2002
G	**NGRIP1.SO4**	**98.6**	**Plummer et al., 2012**
I	GISP2	145	Zielinski, 1995
J	GRIP1	161	Clausen et al., 1997
M	Crete	117	Langway et al., 1988

Table S6b. List of Greenland ice cores used to estimate sulphate flux for Samalas eruption along with corresponding references. Capital letters, in the left column, refer to symbols used to locate each ice core site on Figure S4. Bold letters indicate ice cores not used in previous datasets: GAO07, GAO08 and CR12.

	Name	Sulfate deposition	Reference
A	Dyer	90	Palmer et al., 2002
B	Siple Station	133	Palmer et al., 2002
C	**WDC06A**	**88.6**	**Sigl et al., 2013**
D	**WDC05**	**92.1**	**Sigl et al., 2013**
E	**Byrd**	**24**	**Palmer et al., 2004**
F	*PS1*	*67.6*	*Palmer et al., 2002*
G	SP95	83	Langway et al., 1988
H	**SP04**	**26.3**	**Ferris et al., 2011**
I	**SP84**	**67.6**	**Delmas et al., 1992**
J	SP2001c1	64	Budner et al., 2003
K	DMLS_B32SO4	43	Traufetter et al., 2004
L	**DML05**	**32.5**	**Traufetter et al., 2004**
M	**DML07**	**54.6**	**Traufetter et al., 2004**
N	**DML17**	**49.8**	**Traufetter et al., 2004**
O	**DML03**	**47.3**	**Traufetter et al., 2004**
P	G15	95	Palmer et al., 2002
Q	Plateau Remote	22.39	Palmer et al., 2002
R	**EDC96**	**39.3**	**Castellano et al., 2005**
S	**DT401**	**26.9**	**Ren et al., 2012**
T	*Law Dome*	*57.2*	*Plummer et al., 2012*
U	Hercules Neve	39	Castellano et al., 2005

Table S7a. List of Antarctic ice cores used to estimate sulfate flux for the Tambora eruption along with corresponding references. Capital letters, in the left column, refer to symbols used to locate each ice core site on Figure S4. Bold letters indicate ice cores not used in previous datasets: GAO07, GAO08 and CR12.. Italicized letters indicate ice cores for which values were updated from those used in GAO07, GAO08.

	Name	Sulfate deposition	Reference
A	**Humboldt**	**35.4**	**Sigl et al., 2013**
B	**NEEM-2011-S1**	**39**	**Sigl et al., 2013**
C	Camp Century	63	Clausen et al., 1988
D	GITS	48.4	Mosley et al., 2003
E	NGT_B20	25	Gao et al., 2006
F	North Central	48	Clausen et al., 1988
G	*NGRIP1.SO4*	*40.3*	*Plummer et al., 2012*
H	CsiteE	13	Clausen et al., 1988
I	GISP2	73	Gao et al., 2006
J	**GRIP1**	**39**	**Larsen et al., 2008**
K	**Summit(4 Cores)**	59	**Cole-dai et al., 2009**
L	Greenland Site T	40.6	Mosley et al., 2003
M	Crete	69	Langway et al., 1988
N	CsiteG	94	Clausen et al., 1988
O	CsiteD	129	Clausen et al., 1988
P	CsiteB	71	Clausen et al., 1988
Q	CsiteA	58	Clausen et al., 1988
R	D3	85.4	Mosley et al., 2003
S	D2	52.3	Mosley et al., 2003
T	Raven	55.3	Mosley et al., 2003
U	18C	25	Clausen et al., 1988
V	4B	98	Clausen et al., 1988
W	*Dye3*	*63*	*Larsen et al., 2008*
X	20D	85.4	Gao et al., 2006

Table S7b. List of Greenland ice cores used to estimate sulfate flux for the Tambora eruption along with corresponding references. Capital letters, in the left column, refer to symbols used to locate each ice core site on Figure S4. Bold letters indicate ice cores not used in previous datasets: GAO07, GAO08 and CR12.. Italicized letters indicate ice cores for which values were updated from those used in GAO07, GAO08.

Volcano	Time (CE)		Total number of ice cores			Mean values (kg.km^{-2})			Minimum values (kg.km^{-2})			Maximum values (kg.km^{-2})		
			Greenland	Antarctica	**Total**	Greenland	Antarctica	**Total**	Greenland	Antarctica	**Total**	Greenland	Antarctica	**Total**
Tambora	**1815**	This study	24	21	**45**	57.5	59.2	**116.7**	31.6	30	**61.6**	83.5	88.4	**171.9**
		GAO08	22	18	**40**	59	51	**125.5**						
		CR12	NA	NA	**22**	32.2	52.4	**84.6**						
Samalas	**1257**	This study	7	14	**21**	102.1	94.3	**196.4**	59.9	49.5	**109.4**	144.3	139.1	**283.4**
		GAO08	3	6	**9**	146	112	**258**						
		CR12	NA	NA	**22**	113.6	83.3	**169.9**						

Table S8: Ice core estimates of hemispheric and total sulphate deposition (kg km^{-2}) for Samalas and Tambora eruptions.

	Averaging methods	Mean ($kg.km^{-2}$)	Standard-deviation
Tambora Northern Hemisphere	Simple global average (μ0)	57.55*	25.98
	Climatological regional weighting as in GAO07 (μ1)	57.92	16.94
	Random regional weighting (μ2)	57.2	4.7
Tambora Southern Hemisphere	Simple global average (μ0)	59.20*	29.24
	Climatological regional weighting as in GAO07 (μ1)	59.19	6.22
	Random regional weighting (μ2)	59.4	5.1
Samalas Northern Hemisphere	Simple global average (μ0)	102.10*	42.24
	Climatological regional weighting as in GAO07 (μ1)	102.14	14.7
	Random regional weighting (μ2)	102.9	10.0
Samalas Southern Hemisphere	Simple global average (μ0)	94.29*	44.79
	Climatological regional weighting as in GAO07 (μ1)	94.36	12.01
	Random regional weighting (μ2)	94.0	9.7

Table S9. Mean values and variances obtained using simple hemispheric average (μ0), climatological regional weighting taking into account the regional climatological accumulation rates (μ1) and with a random regional averaging of ice cores (μ2) repeated a thousand times to build a probability density function for each hemisphere. The asterisk (*) next to listed mean values indicates that the null hypothesis (μ0 = μ1) is accepted based on a Student test.

		SO_2 injected (Tg)					Altitude of plume (Km) (US)			Altitude of plume (Km) (LS)			Month
Volcano	Time (CE)	Mean values	Minimum values	Maximum values	GAO07 and	CR12	Minimum	Maximum	70% of mass	Minimum	Maximum	70% of mass	
Tambora	**1815**	56.8 (SC5)	30 (SC4)	83.6 (SC6)	53.5	41.1	19	40	26-33	16	33	22-26	April
Samalas	**1257**	95.5 (SC2)	53.2 (SC1)	137.8 (SC3)	125.5	95.8	29	50	36-43	16	33	22-26	May, July and January

Table S10. Total SO_2 injected (Tg), altitude of injection and month of injection for Samalas and Tambora eruptions.

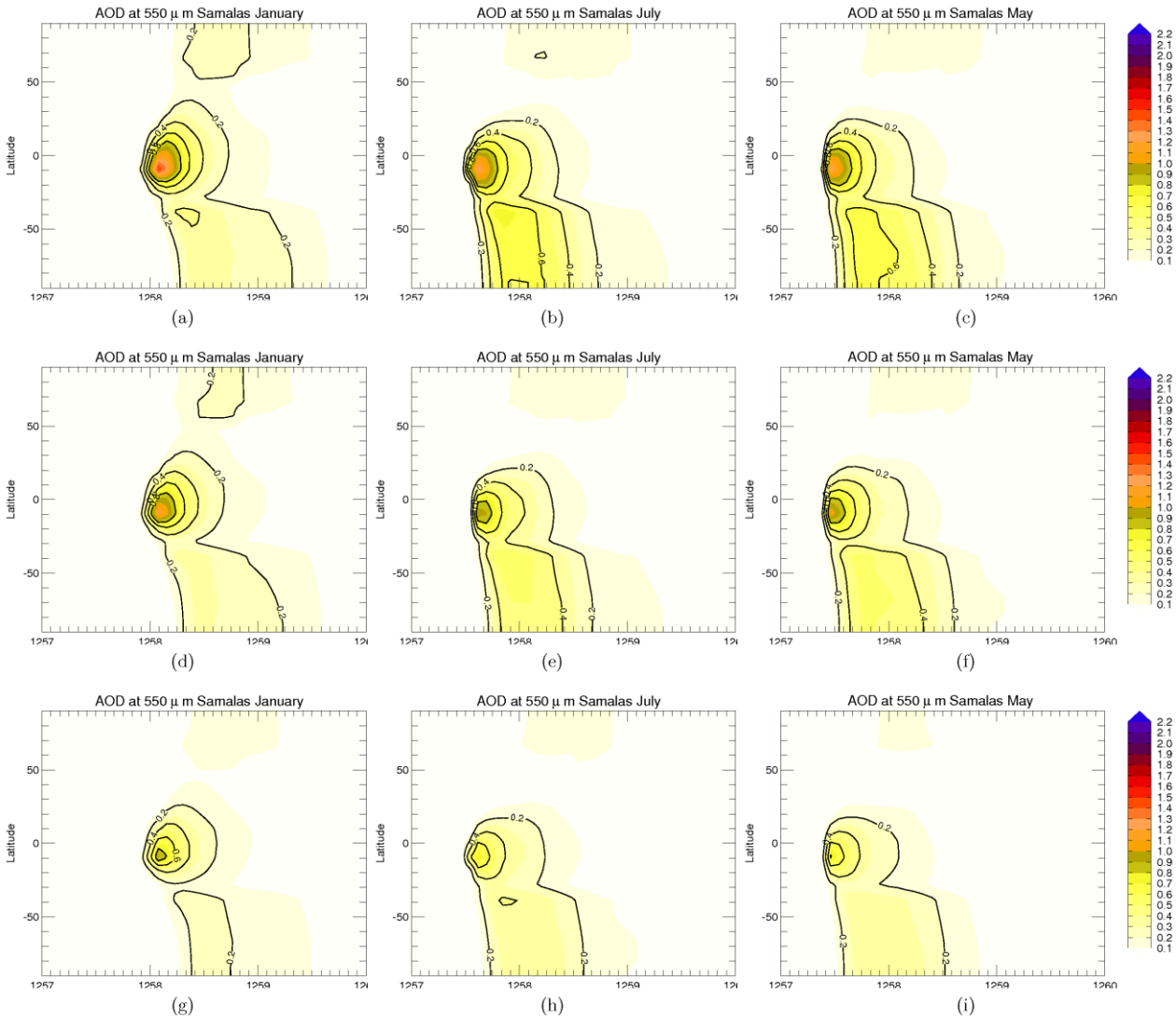

Figure S7. Modelled stratospheric AOD using the (a-b-c) maximum (SC3), (d-e-f) mean (SC2) and (g-h-i) minimum (SC1) scenario of SO_2 loading for Samalas in January (left), May (right) and July (middle) for the lower injection scenario (LS).

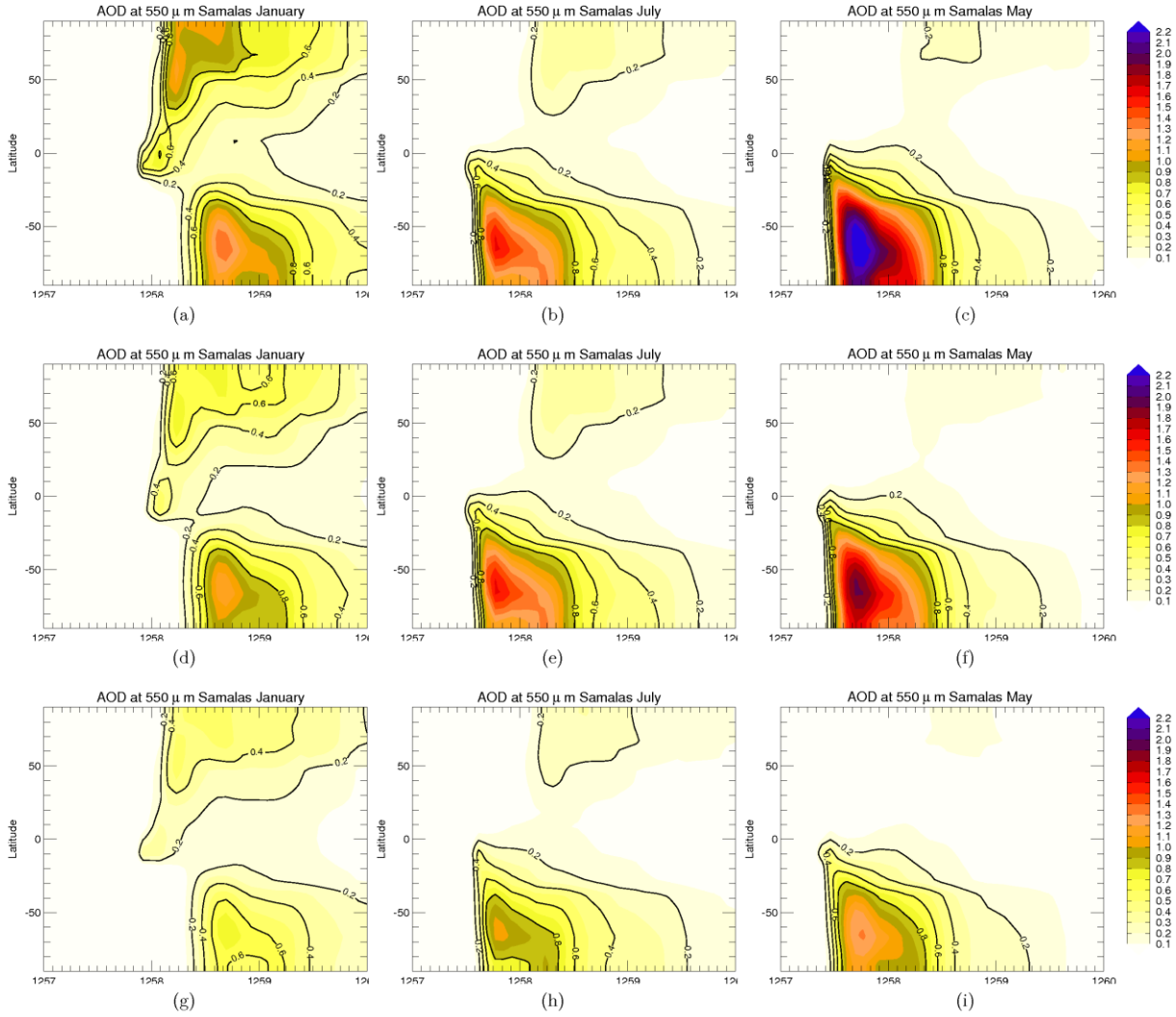

Figure S8. Same as in Figure S7 for Samalas but for the upper injection scenario (US).

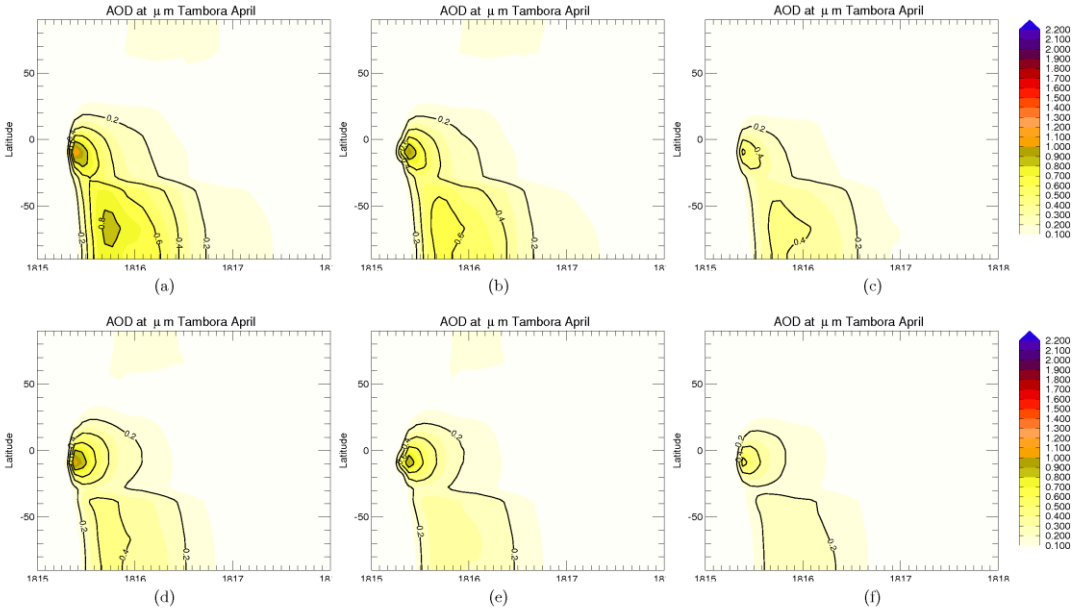

Figure S9. Modelled stratospheric AOD using the (a) maximum (SC6), (b) mean (SC5) and (c) minimum (SC4) scenario of SO_2 loading for Tambora eruption in April for the upper injection (US) scenario. The lower injection (LS) scenarios are shown on the lower panels (d-f).

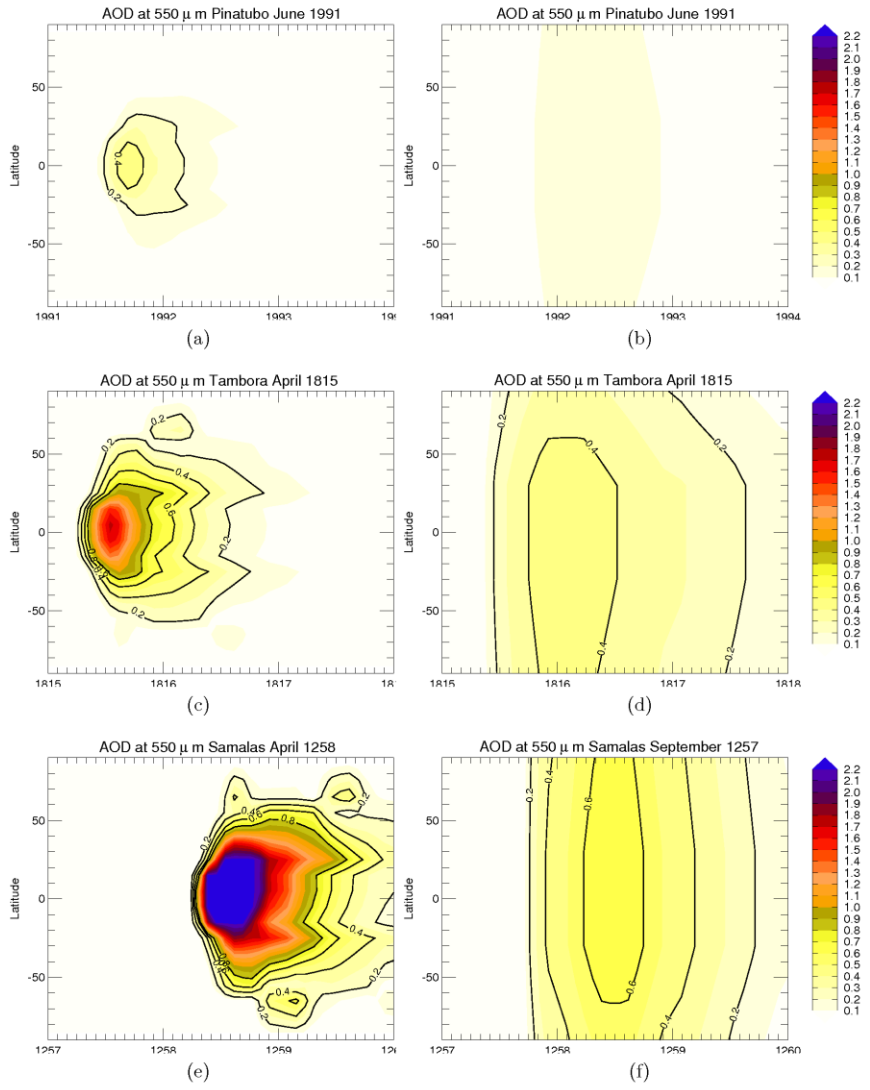

Figure S10. Reconstructed aerosol optical depth (AOD) from Gao et al. (2008) on the left, and from Crowley and Unterman (2013) on the right, for Mt Pinatubo (June 1991), Tambora (April 1815) and Salamas. The Samalas eruption starts in April 1258 in Gao et al. (2008), while the eruption starts in September 1257 in Crowley and Unterman (2013).

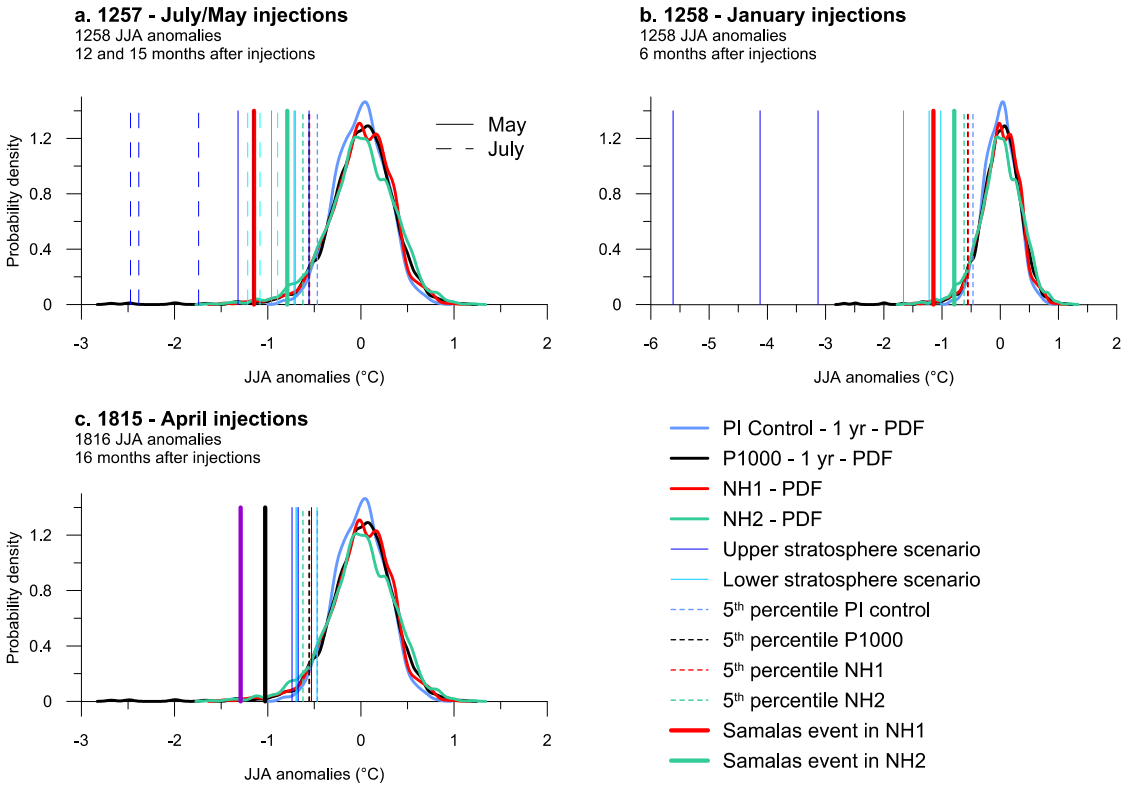

Figure S11. Comparisons between probability density functions (PDFs) from (i) NH1/NH2 reconstructions (red and green), (ii) two millennium-long coupled ocean-atmosphere simulations for either constant pre-industrial condition (PiControl; light blue) or last millennium known forcings (IPSL past1000, P1000; black) and (iii) reconstructed (NH1, NH2) and (iv) simulated (five JJA temperatures sampled randomly) summer cooling induced by the 1257 Samalas eruption with injections starting either in (a) May or July 1257 or (b) January 1258 and (c) by the 1815 Tambora eruption.

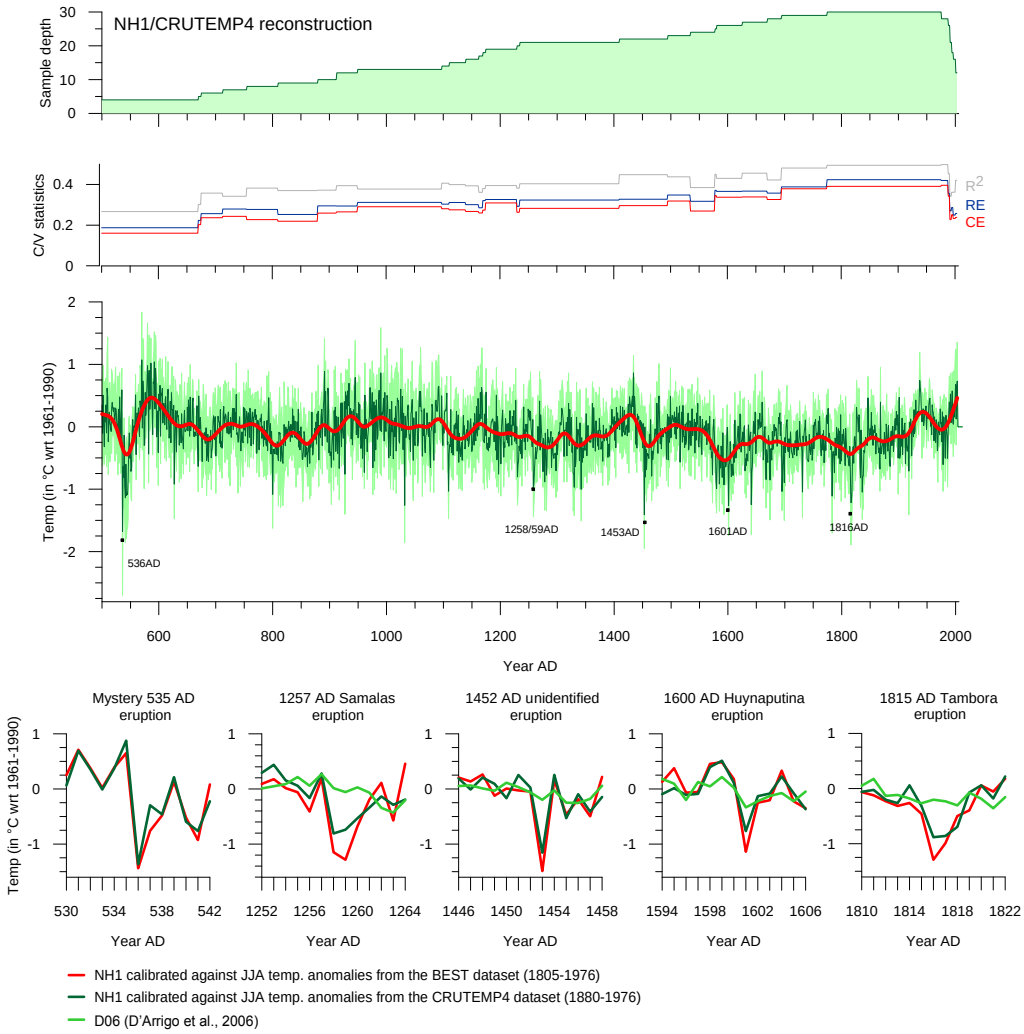

Figure S12. Alternative tree-ring reconstructions of Northern hemisphere (40–90°N) JJA temperature anomalies since 500 and wrt 1961–1990. Reconstruction is composed of 30 clusters (a) sample size, (b) statistics of the reconstructions, (c) the reconstruction is based on 32 nested models and calibrated against instrumental JJA temperatures extracted from the CRUTEM4 gridded dataset (1880-1976). The dark green line represents the reconstructed temperature values, the red curves show the 30-yr smoothing. The envelope in pale green illustrates the 95% confidence interval obtained with the bootstrap approach using 1000 iterations. (d) Comparison of alternative reconstruction with NH1 for the five largest eruptions of the last millennium.

Nest Period	500-670	670-675	675-713	713-755	755-810	810-880	880-913	913-950	950-1098
N Chronologies	4	5	6	7	8	9	10	12	13
p	3	3	4	3	4	4	4	3	3
R2b	0.18[-0.28-0.32]	0.22[-0.22-0.41]	0.26[-0.12-0.44]	0.27[-0.1-0.44]	0.25[-0.14-0.44]	0.24[-0.16-0.41]	0.28[-0.12-0.46]	0.29[-0.03-0.51]	0.31[-0.06-0.47]
r2b	0.27[0.13-0.39]	0.3[0.16-0.43]	0.36[0.23-0.49]	0.34[0.18-0.49]	0.38[0.22-0.49]	0.37[0.23-0.5]	0.37[0.23-0.51]	0.39[0.25-0.52]	0.38[0.22-0.56]
REb	0.19[-0.13-0.32]	0.22[-0.12-0.4]	0.26[-0.11-0.45]	0.28[0.02-0.43]	0.28[-0.02-0.43]	0.25[-0.14-0.43]	0.29[-0.11-0.46]	0.29[-0.04-0.5]	0.31[-0.01-0.48]
CEb	0.16[-0.32-0.3]	0.2[-0.25-0.39]	0.24[-0.15-0.43]	0.24[-0.13-0.42]	0.23[-0.17-0.42]	0.22[-0.2-0.4]	0.26[-0.16-0.45]	0.27[-0.06-0.49]	0.29[-0.09-0.46]

Nest Period	1098-1111	1111-1140	1140-1163	1163-1170	1170-1175	1175-1230	1230-1235	1235-1410	1410-1495
N Chronologies	14	15	16	17	18	19	20	21	22
p	5	5	4	3	3	3	4	4	5
R2b	0.3[-0.37-0.51]	0.29[-0.31-0.47]	0.29[-0.05-0.47]	0.28[-0.22-0.45]	0.29[-0.03-0.48]	0.33[0-0.5]	0.28[0.01-0.47]	0.3[-0.12-0.47]	0.32[-0.01-0.48]
r2b	0.41[0.25-0.57]	0.4[0.26-0.56]	0.39[0.25-0.56]	0.36[0.22-0.51]	0.38[0.25-0.5]	0.39[0.25-0.55]	0.38[0.23-0.54]	0.4[0.27-0.55]	0.45[0.3-0.59]
REb	0.3[-0.23-0.52]	0.31[-0.12-0.48]	0.3[-0.06-0.46]	0.29[-0.15-0.45]	0.32[-0.01-0.48]	0.33[-0.02-0.5]	0.29[0.03-0.47]	0.32[-0.07-0.47]	0.33[0.06-0.5]
CEb	0.28[-0.42-0.5]	0.28[-0.35-0.46]	0.27[-0.08-0.46]	0.26[-0.26-0.44]	0.27[-0.05-0.47]	0.31[-0.03-0.48]	0.26[-0.01-0.46]	0.28[-0.15-0.45]	0.3[-0.05-0.47]

Nest Period	1495-1535	1535-1578	1578-1581	1581-1626	1626-1670	1670-1695	1695-1775	1775-1976	1976-1988
N Chronologies	23	24	25	26	27	28	29	30	28
p	4	3	4	3	5	3	4	6	4
R2b	0.34[-0.03-0.54]	0.29[-0.02-0.45]	0.37[0.13-0.51]	0.36[0.03-0.54]	0.36[0.03-0.55]	0.34[-0.09-0.52]	0.4[-0.14-0.57]	0.41[0.02-0.56]	0.41[0.14-0.54]
r2b	0.44[0.31-0.57]	0.38[0.26-0.5]	0.45[0.31-0.58]	0.43[0.3-0.53]	0.46[0.29-0.57]	0.42[0.3-0.6]	0.48[0.32-0.61]	0.49[0.41-0.65]	0.5[0.34-0.62]
REb	0.35[0.02-0.54]	0.32[-0.02-0.47]	0.37[0.14-0.51]	0.37[0.03-0.53]	0.37[0.07-0.54]	0.36[-0.06-0.52]	0.39[-0.12-0.59]	0.42[0.11-0.57]	0.42[0.19-0.58]
CEb	0.32[-0.05-0.53]	0.27[-0.05-0.43]	0.35[0.11-0.5]	0.34[0-0.52]	0.34[0-0.54]	0.33[-0.12-0.51]	0.38[-0.18-0.56]	0.39[-0.01-0.55]	0.4[0.12-0.53]

Nest Period	1988-1991	1991-1994	1994-1997	1997-2001	2001-2003
N Chronologies	26	21	18	16	12
p	4	3	3	5	6
R2b	0.36[0.09-0.52]	0.25[-0.08-0.43]	0.27[-0.13-0.47]	0.26[-0.23-0.43]	0.26[-0.12-0.47]
r2b	0.45[0.33-0.57]	0.34[0.2-0.49]	0.36[0.22-0.49]	0.36[0.2-0.53]	0.42[0.28-0.55]
REb	0.36[0.07-0.53]	0.27[-0.03-0.44]	0.29[-0.13-0.47]	0.25[-0.11-0.42]	0.26[-0.05-0.48]
CEb	0.34[0.07-0.5]	0.23[-0.12-0.41]	0.25[-0.16-0.46]	0.23[-0.26-0.42]	0.24[-0.16-0.46]

N Chronologies: Number of chronologies
p: Number of principal components
Median value of R2b (1000 bootstrap iterations) calculated over the calibration period
Median value of r2b (1000 bootstrap iterations) calculated over the validation period
Median value of REb: Reduction of error (1000 bootstrap iterations)
Median value of CEb: Coefficient of efficiency (1000 bootstrap iterations)
Numbers in brackets refer to the 2.5th and 97.5th percentiles of the R2, r2, RE, CE distributions

Table S11. Statistics of reconstructed JJA temperature in alternative NH1 reconstruction (calibrated against CRUTEM4 dataset, 1880-1976) for each nest.

Data S1. Evidence for a dry fog in late AD 1257 in England

Matthew Paris and John of Oxnead, two English chroniclers from the 13th century, report the installation of dense fog toward the end of 1257, presumably in October 1257. Its thickness and persistence point to the unusual nature of the phenomenon which can be considered to be a dust veil (or dry fog, i.e. optical phenomena caused by the presence of volcanic aerosols in the troposphere or stratosphere, Stothers, 2002). These testimonies add further confirmation to the recent findings (Lavigne et al., 2013) suggesting an eruption between May and September 1257.

Chronica Majora – Matthew Paris

Annus quoque iste, cronicarum infirmitatum genitivus vix occupatum permisit aliquatenus respirare. Non enim frigus vel serenitas vel gelusaltem aliquantulum stagnorum superficiem, prout consuevit, glacialem induravit, vel stiriam a stillicidiis coegit dependere ; sed continuae inundationes pluviarum et nebularum usque ad Purificationem beatae Virginis aera inspissarunt.

Matthaei Parisiensis monachi sancti Albani Chronica Majora. Luard H.R., ed. (1872–1873), Rerum britannicarum medii aevi scriptores vol. 5 (London), pp. 661–662.

Translation: This year (1257), too, generated chronic complaints, which scarcely allowed free power of breathing to any one laboring under them. Not a single frosty or fine day occurred, nor was the surface of the lakes at all hardened by the frost, as was usual; neither did icicles hang from the ledges of houses; but uninterrupted heavy falls of rain and mist obscured the sky until the Purification of the Blessed Virgin (2 February 1258).

Matthew Paris's English History. From the Year 1235 to 1273. Giles J.A. ed and trans (1854). vol. 3 (Henry G. Bohn, London), pp. 256–257.

Chronica Johannis de Oxenede

Transit annus ista frugifer ac fructifer, sed continuitas pluviarum aestivalium et autumnalium omne genus segetum, fructuum et leguminum suffocavit ita quod ante xlam summa frumenti X solidis venderetur. Aeris igitur intemperies, hominum pestem et mortalitatem suscitavit. [...] Aere spisso et crasso nebulosus ; nec stiria a stillicidius dependebat nec frigus stagnorum rugavit superficiem usque ad beatae Mariae Purificationem ad votum triumphale.

Chronica Johannis de Oxenede, ed. ELLIS H., 1859. Rerum Britannicarum Medii Aevi Scriptores, vol. 13, 439 p.

Translation: Thus passed this year (1257), which should have been fertile and fruitful, but the uninterrupted rain spoiled all the corn, fruits and vegetables in gestation, and at the Advent of our Lord a measure of wheat was sold at 10 shillings. Then the inclemency of the atmosphere brought disease and the death to mankind. [...] The air was dense and obscured by thick fog; neither did icicles hang from the roofs of houses, nor were lake surfaces covered by any ice until the Purification of the Blessed Virgin (i.e. 2 February 1258).

References

AMMANN C. M., JOOS F., SCHIMEL D., OTTO-BLIESNER B. L., TOMAS R., 2007. Solar influence on climate during the past millennium: Results from transient simulations with the NCAR Climate System Model, PNAS, 104, pp. 3713–3718.

ANCHUKAITIS K.J., D'ARRIGO R.D., ANDREU-HAYLES L., FRANK D., VERSTEGE A., BUCKLEY B.M., CURTIS A., JACOBY G.C., COOK E.R., 2012. Tree-ring reconstructed summer temperatures from northwestern North America during the last nine centuries. Journal of Climate, 26, 10, pp. 3001–3012.

ARFEUILLE F., WEISENSTEIN D., MACK H., ROZANOV E., PETER T., BRÖNNIMANN S., 2014. Volcanic forcing for climate modeling: a new microphysics-based data set covering years 1600–present. Climate of the Past 10, 359–375.

BAILLIE M.G.L., 1994. Dendrochronology raises questions about the nature of the AD 536 dust-veil event, The Holocene 4, 2, 212-217.

BAILLIE M.G.L., 2008. Proposed re-dating of the European ice core chronology by seven years prior to the 7th century AD. Geophysical Research Letters, 35, L15813, doi:10.1029/2008GL034755.

BAO Q., LIN P., ZHOU T., LIU Y., YU Y., WU G., HE B., HE J., LI L., LI J., LI Y., LIU H., QIAO F., SONG Z.,WANG B., WANG J., WANG P., WANG X.,WANG Z., WU B., WU T., XU Y., YU H., ZHAO W., ZHENG W., ZHOU L., 2013. The flexible global ocean-atmosphere-land system model, spectral version 2: FGOALS-s2. Advances in Atmospheric Sciences, 30, pp. 561–576.

BEKKI, S., PYLE, J. A., 1992. Two-dimensional assessment of the impact of aircraft sulphur emissions on the stratospheric sulphate aerosol layer. Journal of Geophysical Research: Atmospheres (1984–2012), 97(D14), 15839-15847.

BEKKI, S., PYLE, J. A., 1993. Potential impact of combined NOx and SOx emissions from future high speed civil transport aircraft on stratospheric aerosols and ozone. Geophysical research letters, 20(8), 723-726.

BEKKI S., PYLE J. A., 1994. A two-dimensional modeling study of the volcanic eruption of Mount Pinatubo. Journal of Geophysical Research: Atmospheres (1984–2012), 99(D9), 18861-18869.

BEKKI, S. PYLE J.A., ZHONG W., TOURNI R., HAIGH J.D., PYLE D.M., 1996. The role of microphysical and chemical processes in prolonging the climate forcing of the Toba Eruption. Geophys. Res. Lett. 23, 2669–2672.

BEKKI, S., 1995. Oxidation of volcanic SO2: a sink for stratospheric OH and H2O. Geophysical Research Letters, 22(8), 913-916.

BIGLER, M., WAGENBACH, D., FISCHER, H., KIPFSTUHL, J., MILLER, H., SOMMER, S., STAUFFER, B., 2002. Sulphate record from a northeast Greenland ice core over the last 1200 years based on continuous flow analysis. Annals of Glaciology, 35(1), 250-256.

BOX J. E., BROMWICH D. H., BAI L., 2004. Greenland ice sheet surface mass balance 1991 – 2000: Application of Polar MM5 mesoscale model and in situ data, J. Geophys. Res., 109, D16105, doi:10.1029/2003JD004451.

BRIFFA K.R., JONES P.D., SCHWEINGRUBER F.H., OSBORN T.J., 1998. Influence Of Volcanic Eruptions On Northern Hemisphere Summer Temperature Over The Past 600 Years. Nature, 393, pp. 450-455.

BRIFFA K. R., MELVIN T.M., OSBORN T.J., HANTEMIROV R.M., KIRDYA A.V., MAZEPA V.S., SHIYATOV, S.G., ESPER J., 2013. Reassessing the evidence for tree-growth and inferred temperature change during the Common Era in Yamalia, northwest Siberia. Quaternary Science Reviews, 72, pp. 83-107.

BRIFFA K. R., SHISHOV V. V., MELVIN T. M., VAGANOV E. A., GRUDD H., HANTEMIROV R. M., ERONEN M., NAURZBAEV M. M., 2008. Trends in recent temperature and radial tree growth spanning 2000 years across northwest Eurasia. Philosophical Transactions of the Royal Society B-Biological Sciences, 363, pp. 2271-2284.

BROMWICH D. H., GUO Z. C., BAI L. S., CHEN Q. S. 2004. Modeled antarctic precipitation. Part I: Spatial and temporal variability. J. Climate 17, 427-447.

BUDNER, D., COLE-DAI, J., 2003. The number and magnitude of large explosive volcanic eruptions between 904 and 1865 AD: Quantitative evidence from a new South Pole ice core. Geophysical Monograph Series, 139, 165- 176.

BÜNTGEN U., FRANK D., NIEVERGELT D., ESPER J. 2006. Summer temperature variations in the European Alps, AD 755–2004. Journal of Climate, 19, pp. 606–5623.

BÜNTGEN U., FRANK D. C., GRUDD H., ESPER J., 2008. Long-term summer temperature variations in the Pyrenees. Climate Dynamics, 31, pp. 615–631.

BÜNTGEN U., KYNCL T., GINZLER C., JACKS D.S., ESPER J., TEGEL W., HEUSSNER K.U., KYNCL J., 2013. Filling the Eastern European gap in millennium-long temperature reconstructions. PNAS, 110, pp. 1773-1778.

BUTLER JH, BATTLE M, BENDER ML, MONTZKA SA, CLARKE AD, SALTZMAN ES, SUCHER CM, SEVERINGHAUS JP, ELKINS JW. 1999. A record of atmospheric halocarbons during the twentieth century from polar firn air. Nature, 399, 749–755.

CASTELLANO E., BECAGLI S., HANSSON M., HUTTERLI M., PETIT J. R., RAMPINO M. R., SEVERI M., STEFFENSEN J. P., TRAVERSI R., UDISTI R., 2005. Holocene volcanic history as recorded in the sulfate stratigraphy of the European Project for Ice Coring in Antarctica Dome C (EDC96) ice core. Geophysical Research Letters, vol. 110 (D06), pp. D06114.1-D06114.12, doi:10.1029/2004JD005259.

CLAUSEN, H. B., HAMMER, C. U., 1988. The Laki and Tambora eruptions as revealed in Greenland ice cores from 11 locations. Annals of Glaciology, 10, 16-22.

CLAUSEN H. B., HAMMER C. U., HYIDBERG C. S., DAHL-JENSEN D., STEFFENSEN J. P., KIPFSTUHL J., LEGRAND M., 1997. A comparison of the volcanic records over the past 4000 years from the Greenland Ice Core Project and Dye 3 Greenland ice cores J. Geophys. Res., 26,707-26,723.

COLE-DAI J., MOSLEY-THOMPSON E., WIGHT S. P., THOMPSON L.G., 2000. A 4100-year record of explosive volcanism from an East Antarctica ice core, J. Geophys. Res., 105, 24,431 – 24,441.

COLE-DAI J., FERRIS D., LANCIKI A., SAVARINO J., BARONI M., THIEMENS M.H., 2009. Cold decade (AD 1810– 1819) caused by Tambora (1815) and another (1809) stratospheric volcanic eruption, Geophysical Research Letters, 36, L22703, doi:10.1029/2009GL040882.

COLE-DAI J., FERRIS D.G., LANCIKI A.L., SAVARINO J., THIEMENS M.H., MCCONNELL J.R., 2013. Two likely stratospheric volcanic eruptions in the 1450s CE found in a bipolar, subannually dated 800 year ice core record. Journal of Geophysical Research-Atmospheres, 118, 14, 7459–7466.

COOK E. R., MEKO D. M., STAHLE D. W., CLEAVELAND M. K., 1999. Drought reconstructions for the continental United States. Journal of Climate, 12, pp. 1145–1162.

CORONA C., EDOUARD J.L., GUIBAL F., GUIOT J., BERNARD S., THOMAS A., DENELLE N., 2011. Long-term summer (751-2008) temperature fluctuation in the French Alps based on tree-ring data. Boreas, 40, 351-366.

CORONA C., GUIOT J., EDOUARD J.L., CHALIÉ F., BÜNTGEN U., NOLA P., URBINATI C., 2010. Millennium-long summer temperature variations in the European Alps as reconstructed from tree rings. Climate of the Past, 6, 379-400.

CROWLEY T. J., Unterman M. B., 2013. Technical details concerning development of a 1200 yr proxy index for global volcanism. Earth Syst. Sci. Data. 5, 187–197.

CROWLEY T. J., ZIELINSKI G., VINTHER B., UDISTI R., KREUTZ K., COLE-DAI J., CASTELLANO E., 2008. Volcanism and the Little Ice Age. PAGES Newsletter, 16, pp. 22–23.

D'ARRIGO, R. D., JACOBY G. C., BUCKLEY B. M., SAKULICH J., FRANK D., WILSON R., CURTIS A., ANCHUKAITIS K.J., 2009. Tree growth and inferred temperature variability at the North American Arctic treeline. Global and Planetary Change, 65, (1-2), pp. 71–82.

D'ARRIGO R., WILSON R., JACOBY G., 2006. On the long-term context for late twentieth century warming. Journal of Geophysical Research, 111, D03103, doi:10.1029/2005JD006352.

D'ARRIGO R., MASHIG E., FRANK D., WILSON R.J.S., JACOBY G., 2005. North Pacific-Related Climate Variability Inferred from Seward Peninsula, Alaska Tree Rings since A.D. 1358. Climate Dynamics, 24, pp. 227-236.

D'ARRIGO R., JACOBY G., FRANK D., PEDERSON N., COOK E., BUCKLEY B., NACHIN B., MIJIDDORJ R., DUGARJAV C., 2001. 1738 years of Mongolian Temperature Variability Inferred from a Tree-Ring width Chronology of Siberian Pine. Geophysical Research Letters, 23, 3, pp. 543-546.

DELAYGUE G., BARD E., 2011. An Antarctic view of beryllium-10 and solar activity for the past millennium. Climate Dynamics, 36, pp. 2201–2218.

DELMAS R. J., KIRCHNER S., PALAIS J. M., PETIT J. R.., 1992. 1000 years of explosive volcanism recorded at the South Pole. Tellus B, 44(4), pp. 335-350.

DEMORE W. B., MARGITAN J. J., MOLINA M. J., WATSON R. T., GOLDEN D. M., HAMPSON R. F., KURYLO M. J., HOWARD C. J., RAVISHANKARA A. R., 1990. Chemical kinetics and photochemical data for use in stratospheric model, Evaluation 9, NASA/JPL Publ., 90-1.

DUFRESNE, J.-L., AND COAUTHORS, 2013. Climate change projections using the IPSL-CM5 Earth System Model: From CMIP3 to CMIP5. Climate Dynamics, 40, pp. 2123–2165.

DULL R., SOUTHON J. R., KUTTEROLF S., FREUNDT A., WAHL D., SHEETS P., 2010. Did the TBJ Ilopango eruption cause the AD 536 event? American Geophysical Union, Fall Meeting 2010.

ESPER J., SCHNEIDER L., KRUSIC P.J., LUTERBACHER J., BÜNTGEN U., TIMONEN M., SIROCKO F., ZORITA E., 2013. European summer temperature response to annually dated volcanic eruptions over the past nine centuries. Bulletin of Volcanology, 75, 736, doi: 10.1007/s00445-013-0736-z

ESPER J., BÜNTGEN U., TIMONEN M., FRANK D.C., 2012b. Variability and extremes of Northern Scandinavian summer temperatures over the past two millennia. Global and Planetary Change, 88-89, 1-9.

ESPER J., FRANK D.C., TIMONEN M., ZORITA E., WILSON R.J.S., LUTERBACHER J., HOLZKÄMPER S., FISCHER N., WAGNER S., NIEVERGELT D., VERSTEGE A., BÜNTGEN U., 2012a. Orbital forcing of tree-ring data. Nature Climate Change, 2, 862-866.

FERRIS D. G., COLE-DAI J., REYES A. R., BUDNER D. M., 2011. South Pole ice core record of explosive volcanic eruptions in the first and second millennia A.D. and evidence of a large eruption in the tropics around 535 A.D., J. Geophys. Res., 116, 1–11.

GAO C., ROBOCK A., SELF S., WITTER J.B., STEFFENSON J.P., CLAUSEN H.B., M. L. SIGGARD ANDERSON M.L., JOHNSEN S., MAYEWSKI P.A., AMMANN C., 2006. The 1452 or 1453 AD Kuwae eruption signal derived from multiple ice core records: Greatest volcanic sulfate event of the past 700 years. Journal of Geophysical Research, vol. 111, D12107, doi: 10.1029/2005JD006710.

GAO C., OMAN L., ROBOCK A., STENCHIKOV G. L., 2007. Atmospheric volcanic loading derived from bipolar ice cores: Accounting for the spatial distribution of volcanic deposition. Journal of Geophysical Research, 112(D9).

GAO C., ROBOCK A., AMMANN C., 2008. Volcanic forcing of climate over the past 1500 years: An improved ice core-based index for climate models. Journal of Geophysical Research, vol. 113, D23111, 15 PP, doi: 10.1029/2008JD010239.

GENNARETTI F., ARSENEAULT D., NICAULT A., PERREAULT L., BÉGIN Y., 2014. Volcano-induced regime shifts in millennial tree ring chronologies from Northeastern North America. PNAS, 111, pp. 10077-10082.

GENT P. R., DANABASOGLU G., DONNER L., HOLLAND M., HUNKE E., JAYNE S., LAWRENCE D., NEALE R., RASCH P., VERTENSTEIN M., WORLEY P., YANG Z.-L., ZHANG M., 2011. The Community Climate System Model version 4, Journal of Climate, 24, pp. 4973–4991, doi:10.1175/2011JCLI4083.1.

HARWOOD R. S., PYLE J. A., 1975. A two-dimensional mean circulation model for the atmosphere below 80km. Q. J. R. Meteorol. Soc. 101, 723–747.

KIRCHHEFER, A. J., 2001. Reconstruction of summer temperatures from tree-rings of Scots pine (Pinus sylvestris L.) in coastal northern Norway, Holocene, 11, pp. 41–52.

LANGWAY J.R., C. C. CLAUSEN H. B., HAMMER C. U., 1988. An inter-hemispheric volcanic time-marker in ice cores from Greenland and Antarctica. Annals of Glaciology, 10, pp. 102-108.

LANGWAY C. C., OSADA K., CLAUSEN H. B., HAMMER C. U., SHOJI H., MITANI A., 1994. New chemical stratigraphy over the last millennium for Byrd Station, Antarctica, Tellus, Ser. B, 46, 40 – 51.

LARSEN L. B., VINTHER B. M., BRIFFA K. R., MELVIN T. M., CLAUSEN H. B., JONES P. D., SIGGAARD-ANDERSEN, M.-L., HAMMER C. U., ERONEN M., GRUDD H., GUNNARSON B. E., HANTEMIROV R.M., NAURZBAEV M. M., NICOLUSSI K., 2008. New ice core evidence for a volcanic cause of the AD 536 dust veil. Geophysical Research Letters, vol. 35, L04708, doi:10.1029/2007GL032450.

LAVIGNE F., DEGEAI J.P., KOMOROWSKI J.C., GUILLET S., LAHITTE P., ROBERT V., OPPENHEIMER C., STOFFEL M., VIDAL C.M., WASSMER P., HAJDAS I., HADMOKO D.S., PRATOMO I., DE BÉLIZAL E., SURONO, 2013. Source of the Great AD 1257 Mystery Eruption Unveiled, Samalas Volcano, Rinjani Volcanic Complex, Indonesia. PNAS, 110(42), pp. 16742–16747.

LAW K.S., PYLE J.A., 1993. Modeling trace gas budgets in the troposphere: 1. Ozone and odd nitrogen. J. Geophys. Res. 98, 18377.

LORENZ E.N., 1959. Empirical orthogonal functions and statistical weather prediction, Scientific Report 1, Massachusetts Institute of Technology, Cambridge, p. 57.

LUCKMAN B. H., WILSON R.J.S., 2005. Summer temperature in the Canadian Rockies during the last millennium – a revised record. Climate Dynamics, 24, pp. 131-144.

MARSLAND S.J., HAAK H., JUNGCLAUS J.H., LATIF M., RÖSKE F., 2003. The Max-Planck-Institute global ocean/sea ice model with orthogonal curvilinear coordinates. Ocean Modelling, 5(2), pp. 91-127

Mc CORMICK MP, VEIGA RE. 1992. SAGE II measurements of early Pinatubo aerosols. Geophysical Research Letters, 19, 155–158.

MELVIN T.M., GRUDD H., BRIFFA K.R., 2012. Potential bias in 'updating' tree-ring chronologies using regional curve standardisation: Re-processing 1500 years of Torneträsk density and ring-width data. Holocene, 23, pp. 364-373.

MOSLEY-THOMPSON E., MASHIOTTA T. A., THOMPSON L. G., 2003. High resolution ice core records of late Holocene volcanism: Current and future contributions from the Greenland PARCA core. Geophysical Monograph Series, 139, pp. 153-164.

NAURZBAEV M.M., VAGANOV E.A., SIDOROVA O.V., SCHWEINGRUBER, F.H., 2002. Summer temperatures in eastern Taimyr inferred from a 2427-year late-Holocene tree-ring chronology and earlier floating series. The Holocene 12, 727-736.

OMAN L., ROBOCK A., STENCHIKOV G., THORDARSON T., 2006. High-latitude eruptions cast shadow over the African monsoon and the flow of the Nile. Geophysical Research Letter, 33, L18711, doi: 10.1029/2006GL027665

OPPENHEIMER C., 2003a. Ice core and palaeoclimatic evidence for the timing and nature of the great mid-13th century volcanic eruption. International Journal of Climatology, 23, 4, pp. 417–426.

OPPENHEIMER C., 2003b. Climatic, environmental and human consequences of the largest known historic eruption: Tambora volcano (Indonesia) 1815. Progress in Physical Geography, 27, pp. 230-259.

PALMER A. S., MORGAN V. I., CURRAN M. A., VAN OMMEN T. D., MAYEWSKI P. A., 2002. Antarctic volcanic flux ratios from Law Dome ice cores. Annals of Glaciology, 35(1), pp. 329-332.

PALMER, M. A., GRAY, L. J., ALLEN, M. R., NORTON, W. A., 2004. Solar forcing of climate: model results. Adv. Space Res., 34, 343–348.

PHIPPS S. J., 2010. The CSIRO Mk3L climate system model v1.2. Technical Report No. 4, Antarctic Climate & Ecosystems CRC, Hobart, Tasmania, Australia, 122 pp., ISBN 978-1-921197-04-8.

PLUMMER, C. T., CURRAN, M. A. J.; VAN OMMEN, T. D., RASMUSSEN, S. O., MOY, A. D., VANCE, T. R., CLAUSEN, H. B., VINTHER, B. M., MAYEWSKI, P. A., 2012. An independently dated 2000-yr volcanic record from Law Dome, East Antarctica, including a new perspective on the dating of the c. 1450s eruption of Kuwae, Vanuatu. Climate of the Past Discussions, 8, 3, 2012, pp. 1567-1590.

POPA I., KERN Z., 2009. Long-term summer temperature reconstruction inferred from tree-ring records from the Eastern Carpathians. Climate Dynamics, 32, pp. 1107–1117.

RADDATZ T. J., REICK C. H., KNORR W., KATTGE J., ROECKNER E., SCHNUR R., SCHNITZLER K.G.,WETZEL P., JUNGCLAUS J., 2007. Will the tropical land biosphere dominate the climate-carbon feedback during the twenty- first century? Climate Dynamics, 29, pp. 565–574.

READ WG., FROIDEVAUX L., WATERS JW., 1993. Microwave limb sounder measurement of stratospheric SO_2 from the Mt. Pinatubo Volcano. Geophysical Research Letters, 20, 1299–1302.

REN J., LI C., HOU S., XIAO C., QIN D., LI Y., DING M., 2010. A 2680 year volcanic record from the DT-401 East Antarctic ice core. Journal of Geophysical Research, 115(D11).

SANDER S.P. et al., 2011. Chemical Kinetics and Photochemical Data for Use inAtmospheric Studies, Evaluation," JPL Publication (10–6, JPL Publication, Pasadena, 2011), (available at http://jpldataeval.jpl.nasa.gov/).

SAVARINO J., 2003. UV induced mass-independent sulfur isotope fractionation in stratospheric volcanic sulfate. Geophys. Res. Lett. 30, doi:10.1029/2003GL018134.

SCHMIDT G.A., RUEDY R., HANSEN J. E., ALEINOV I., BELL N., BAUER M., BAUER S., CAIRNS B., CANUTO V., CHENG Y., DEL GENIO A., FALUVEGI G., FRIEND A.D., HALL T.M., HU Y., KELLEY M., KIANG N.Y., KOCH D., LACIS A.A., LERNER J., LO K.K., MILLER R.L., NAZARENKO L., OINAS V., PERLWITZ J., PERLWITZ J., RIND D., ROMANOU A., RUSSELL G.L., SATO M., SHINDELL D.T., STONE P.H., SUN S., TAUSNEV N., THRESHER D., YAO M.-S., 2006. Present day atmospheric simulations using giss modele: Comparison to in-situ, satellite and reanalysis data. Journal of Climate, 19, pp. 153–192.

SELF S., GERTISSER R., THORDARSON T., RAMPINO M. R., WOLFF J.A., 2004. Magma volume, volatile emissions, and stratospheric aerosols from the 1815 eruption of Tambora. Geophysical Research Letters, 31(20), L20608.

SIDOROVA O.V., NAURZBAEV, M.M., 2002. Response of Larix cajanderi to climatic changes at the Upper Timberline and in the Indigirka River Valley. Lesovedenie 2, 73—75.

SIGL M., MCCONNELL J. R., LAYMAN L., MASELLI O., MCGWIRE K., PASTERIS D., DAHL-JENSEN D., STEPHANSON J. P., VINTHER B. M., EDWARDS R., MULVANEY R., KIPFSTUHL, S., 2013. A new bipolar ice core record of volcanism from WAIS Divide and NEEM and implications for climate forcing of the last 2000 years. Journal of Geophysical Research, 118(3), pp. 1151-1169.

SIGURDSSON H., CAREY S., 1989. Plinian and co-ignimbrite tephra fall from the. Bulletin of Volcanology, 51(4), 243-270.

SPARC, 2006. SPARC Assessment of Stratospheric Aerosol Properties (ASAP), Tech. Rep. WMO-TD No. 1295, WCRP Series Report No. 124, SPARC Report No. 4, Berrieres le Buisson Cedex.

STEINHILBER F., BEER J., FROHLICH C., 2009. Total solar irradiance during the Holocene. Geophysical Research Letters, 36, L19704, doi:10.1029/2009GL040142.

STOTHERS R. B., 1984. The Great Tambora Eruption in 1815 and its aftermath. Science, 224 (4654), pp. 1191- 1198.

STOTHERS R.B., 2000. Climatic and Demographic Consequences of the Massive Volcanic Eruption of 1258. Clim. Change 45, 361–374.

STOTHERS R.B., 2002. Cloudy and clear stratospheres before A. D. 1000 inferred from written sources. Journal of Geophysical Research, vol. 107(D23), 4718, doi:10.1029/2002JD002105

THORDARSSON T., SELF S., 2003. Atmospheric and environmental effects of the 1783–1784 Laki eruption: a review and reassessment. Journal of Geophysical Research, vol.108 (D1) 4011, doi:10.1029/2001JD002042.

TRAUFETTER F., OERTER H., FISCHER H., WELLER R., MILLER H., 2004. Spatio-temporal variability in volcanic sulphate deposition over the past 2 kyr in snow pits and firn cores from Amundsenisen, Antarctica. Journal of Glaciology, 50(168), pp. 137-146.

VIEIRA, L. E. A., SOLANKI S.K., 2010. Evolution of the solar magnetic flux on time scales of years to millenia, Astronomy and Astrophysics, 509, A100, doi:10.1051/0004-6361/200913276.

WANG Y.M., LEAN J. L., SHEELEY N. R. JR., 2005. Modeling the Sun's Magnetic Field and Irradiance since 1713, The Astrophysical Journal, 625, pp. 522–538, doi:10.1086/429689.

WATANABE S., HAJIMA T., SUDO K., NAGASHIMA T., TAKEMURA T., OKAJIMA H., NOZAWA T., KAWASE H., ABE M., YOKOHATA T., ISE, T., SATO, H., KATO, E., TAKATA, K., EMORI, S., AND KAWAMIYA, M., 2010. MIROC-ESM: model description and basic results of CMIP5-20c3m experiments. Geoscientific Model Development, 4, pp. 845-872.

WILSON R., WILES G., D'ARRIGO R., ZWECK C., 2007. Cycles and Shifts: 1300-years of multi-decadal temperature variability in the Gulf of Alaska. Climate Dynamics, 28, pp. 425–440.

WITTER J.B., SELF S., 2007. The Kuwae (Vanuatu) eruption of AD 1452: potential magnitude and volatile release. Bulletin of Volcanology, 69, pp. 301-318.

WU, T., LI, W., JI, J., XIN, X., LI, L., WANG, Z., ZHANG, Y., LI, J., ZHANG, F., WEI, M., SHI, X., WU, F., ZHANG, L., CHU, M., JIE, W., LIU, Y., WANG, F., LIU, X., LI, Q., DONG, M., LIU, Q., AND ZHANG, J., 2013. Global carbon budgets simulated by the Beijing Climate Center Climate System Model for the last century, Journal of Geophysical Research, 118, pp. 4326–4347, doi:10.1002/jgrd.50320.

ZIELINSKI G. A., 1995. Stratospheric loading and optical depth estimates of explosive volcanism over the last 2100 years derived from the Greenland Ice Sheet Project 2 ice core. Journal of Geophysical Research, 100(D10), pp. 20937-20955.